Trace element geochemistry (Li, Ba, Sr, and Rb) using *Curiosity*'s ChemCam: Early results for Gale crater from Bradbury Landing Site to Rocknest

Ann M. Ollila,[1] Horton E. Newsom,[1] Benton Clark III,[2] Roger C. Wiens,[3] Agnes Cousin,[3] Jen G. Blank,[4] Nicolas Mangold,[5] Violaine Sautter,[6] Sylvestre Maurice,[7] Samuel M. Clegg,[3] Olivier Gasnault,[7] Olivier Forni,[7] Robert Tokar,[8] Eric Lewin,[9] M. Darby Dyar,[10] Jeremie Lasue,[7] Ryan Anderson,[11] Scott M. McLennan,[12] John Bridges,[13] Dave Vaniman,[8] Nina Lanza,[3] Cecile Fabre,[14] Noureddine Melikechi,[15] Glynis M. Perrett,[16] John L. Campbell,[16] Penelope L. King,[16,17] Bruce Barraclough,[8] Dorothea Delapp,[3] Stephen Johnstone,[3] Pierre-Yves Meslin,[7] Anya Rosen-Gooding,[18] Josh Williams,[1] and The MSL Science Team

[1]   The ChemCam instrument package on the Mars rover, *Curiosity*, provides new capabilities to probe the abundances of certain trace elements in the rocks and soils on Mars using the laser-induced breakdown spectroscopy technique. We focus on detecting and quantifying Li, Ba, Rb, and Sr in targets analyzed during the first 100 sols, from Bradbury Landing Site to Rocknest. Univariate peak area models and multivariate partial least squares models are presented. Li, detected for the first time directly on Mars, is generally low (<15 ppm). The lack of soil enrichment in Li, which is highly fluid mobile, is consistent with limited influx of subsurface waters contributing to the upper soils. Localized enrichments of up to ~60 ppm Li have been observed in several rocks but the host mineral for Li is unclear. Bathurst_Inlet is a fine-grained bedrock unit in which several analysis locations show a decrease in Li and other alkalis with depth, which may imply that the unit has undergone low-level aqueous alteration that has preferentially drawn the alkalis to the surface. Ba (~1000 ppm) was detected in a buried pebble in the Akaitcho sand ripple and it appears to correlate with Si, Al, Na, and K, indicating a possible feldspathic composition. Rb and Sr are in the conglomerate Link at abundances >100 ppm and >1000 ppm, respectively. These analysis locations tend to have high Si and alkali abundances, consistent with a feldspar composition. Together, these trace element observations provide possible evidence of magma differentiation and aqueous alteration.

[1]Institute of Meteoritics, Department of Earth and Planetary Sciences, Albuquerque, New Mexico, USA.

[2]Space Science Institute, Boulder, Colorado, USA.

[3]Los Alamos National Laboratory, Los Alamos, New Mexico, USA.

[4]NASA Ames Research Center, Moffett Field, California, USA.

[5]LPGN, CNRS, UMR6112, Université Nantes, Nantes, France.

[6]Laboratoire de Minéralogie et Cosmochimie du Muséum, Muséum National d'Histoire Naturelle, Paris, France.

[7]Institut de Recherche en Astrophysique et Planétologie, Université Paul Sabatier, Toulouse, France.

[8]Planetary Science Institute, Tucson, Arizona, USA.

[9]ISTerre, Grenoble, France.

[10]Department of Astronomy, Mount Holyoke College, South Hadley, Massachusetts, USA.

[11]Astrogeology Science Center, U.S. Geological Survey, Flagstaff, Arizona, USA.

[12]Department of Geosciences, State University of New York at Stony Brook, Stony Brook, New York, USA.

[13]Space Research Centre, Department of Physics and Astronomy, University of Leicester, Leicester, UK.

[14]GeoResources, CNRS, UMR7356, Université de Lorraine, Vandoeuvre lès Nancy, France.

[15]Optical Science Center for Applied Research, Delaware State University, Dover, Delaware, USA.

[16]Department of Physics, University of Guelph, Guelph, Ontario, Canada.

[17]Research School of Earth Sciences, Australian National University, Canberra, ACT, Australia.

[18]Albuquerque Academy, Albuquerque, New Mexico, USA.

Corresponding author: A. M. Ollila, Institute of Meteoritics, Department of Earth and Planetary Sciences, 1 University of New Mexico, MSC03-2050, Albuquerque, NM 87131-0001, USA. (aollila@unm.edu)

1. Introduction

1.1. Mission Overview

[2] On 6 August 2012, the Mars Science Laboratory (MSL) rover, *Curiosity*, successfully touched down on the surface of Mars, just northwest of the central mound, Mount Sharp, in Gale crater. The primary objective of *Curiosity*'s mission is to characterize the geology and atmosphere in Gale crater and search for habitable environments or locations that sustain or may have sustained life in the past [*Grotzinger et al.*, 2012]. *Curiosity* landed on what appears to be the distal end of an alluvial fan, based on orbital geomorphology [*Anderson and Bell*, 2010] and the presence of material consistent with a fluvial conglomerate [*Williams et al.*, 2013]. Over the first 100 sols, the rover traveled ~400 m and descended ~15 m from Bradbury Landing Site to a location called Rocknest in the Glenelg region where three distinct geologic units meet [*Grotzinger et al.*, 2013]. Note that all of the small-scale feature names in this paper are informal and are not approved by the International Astronomical Union.

[3] There are two emission spectroscopy instruments on the rover that provide complementary chemical information on rocks and soils: the ChemCam and Alpha Particle X-Ray Spectrometer (APXS). Note that the term Martian soil is used here to denote any loose, unconsolidated materials that can be distinguished from rocks, bedrock, or strongly cohesive sediments. No implication of the presence or absence of organic materials or living matter is intended, nor is the genesis of the deposit. The ChemCam instrument suite has a laser-induced breakdown spectrometer (LIBS) and a remote micro-imager (RMI), and this is the first planetary mission to use a LIBS instrument [*Wiens et al.*, 2012; *Maurice et al.*, 2012]. ChemCam is a remote instrument designed to operate at distances of 1.5 to 7 m from the rover. It can detect, dependent on the concentration, all major elements (Si, Ca, Mg, Al, K, Na, Ti, and Fe), several minor elements (H, C, N, P, S, Cl, and Mn), and many trace elements (Li, B, Rb, Sr, Ba, Cr, Ni, Cu, Zn, As, Cd, and Pb). Major element calibration and some minor and trace element detections for ChemCam are discussed by *Wiens et al.* [2013].

[4] APXS is a contact instrument that is placed on or very near the surface to be analyzed. APXS instruments were used on the Mars Pathfinder mission [*Rieder et al.*, 1997] and the Mars Exploration Rovers (MER), Spirit and Opportunity [*Rieder et al.*, 2003]. *Curiosity*'s APXS instrument can detect all major elements, several minor elements (Mn, P, S, and Cl), and many trace elements dependent on the concentration (Rb, Sr, Ba, V, Cr, Co, Ni, Cu, Zn, Ga, Ge, and As) [*Campbell et al.*, 2012]. Due to peak overlap, APXS has difficulty quantifying Ba and it cannot detect Li [*Campbell et al.*, 2012].

[5] In this study, we focus on trace element calibrations for elements that are readily detectable by ChemCam at low (<100 ppm) concentrations and for which sufficient data collected using the ChemCam flight model (now on Mars) are available to use for preliminary modeling: Li, Ba, Sr, and Rb. The most accurate univariate and partial least squares (PLS) models are used to provide abundances for Mars targets and, when applicable, the results are compared to APXS abundances. These results are the first in situ Li and Ba abundances for Mars.

1.2. Geological Significance

[6] Trace element observations of Li, Ba, Rb, and Sr may provide clues to the origin of igneous rocks and the abundances of fluid mobile trace elements (e.g., Li and Ba) may also provide clues to identifying alteration processes that a rock could have been exposed to on or near the surface. Li preferentially remains in a basaltic melt as crystallization occurs and replaces Mg in pyroxene crystals forming from the residual melt; hence, they may become enriched (up to ~100 ppm) in Li [e.g., *Su et al.*, 2012]. Li is also used as a chemical signature due to its high mobility in fluids [*Newsom et al.*, 1999] and it may be a key indicator to determine if the salt component of the Martian soils [*Clark et al.*, 1982] is due to vapor deposition or hydrothermal processes [*Newsom et al.*, 1999]. Some clay minerals retain Li, either in the mineral structure or adsorbed in the interlayer region [e.g., *Horstman*, 1957]. During crystallization, Ba^{2+} substitutes for K^+ in the alkali feldspar structure where it is generally charge balanced by $Ba^{2+} + Al^{3+} = K^+ + Si^{4+}$. Surfaces of rocks may become enriched in Ba through alteration processes, e.g., in rock varnishes [*Garvie et al.*, 2008]. The ionic radii of Rb^+ and K^+ are approximately the same size and these ions are of the same valence state. Rb will substitute for K in the feldspar and mica mineral structures [e.g., *Shaw*, 1968], and the ratio of K/Rb can indicate the amount of fractionation, weathering, hydrothermal alteration, diagenesis, or metamorphism the material has undergone [e.g., *Shaw*, 1968; *Nath et al.*, 2000; *Wronkiewicz and Condie*, 1990]. Sr tends to remain in a basaltic melt during fractional crystallization (i.e., the partition coefficient, K_d, for Sr in most of the crystallizing minerals like olivine, pyroxene, and plagioclase is much greater than one). In more felsic compositions (where K_d is closer to 1), Sr substitutes for Ca in plagioclase, hornblende, micas, and pyroxene.

1.3. Previous Detections on Mars

[7] The capability to detect Rb and Sr was available on the 1977 Viking landers. Each lander had an X-ray fluorescence (XRF) spectrometer capable of detecting Rb and Sr at levels ≥ 30 ppm [*Toulmin et al.*, 1977]. The soil samples they analyzed did not show Rb concentrations above this detection limit, and they found Sr concentrations of 60 ± 30 ppm and 100 ± 40 ppm in two soil samples. *Toulmin et al.* [1977] interpreted these concentrations to be consistent with primitive, non-granitic, source material. Pathfinder and the MERs had APXS instruments capable of nominally detecting Sr, Ba, and Rb. Due to the difficulty in analyzing the scatter peaks that overlap peaks from these elements, no information is currently available from these missions for these elements.

1.4. Mars Meteorite Detections

[8] Whole rock Rb concentrations in the Mars meteorites are under 15 ppm [e.g., *Nakamura*, 1982; *Ruzicka et al.*, 2001; *Borg et al.*, 1997, 2002; *Borg and Draper*, 2003]. *Bridges and Grady* [2000] found Rb abundances up to 46 ppm in siderite grains and 17.7 ppm in clays in the Lafayette meteorite. *Agee et al.* [2013] found up to 75 ppm Rb in the light-toned material separates of NWA 7034, which are thought to be feldspar and Cl apatite. Sr values up to 110 ppm were observed in plagioclase grains in the basaltic shergottite QUE 94201 [*Borg et al.*, 1997]. Concentrations of Sr up to 1050 ppm were seen in siderite grains and up to

929 ppm in clays in Lafayette [*Bridges and Grady*, 2000]. A compilation of Ba concentrations in shergottites by *Ruzicka et al.* [2001] shows average whole rock concentrations of 16.4 ± 11.8 ppm. *Bridges and Grady* [2000] observed Ba concentrations up to 106 ppm in Governador Valadares siderite grains and up to 36.6 ppm in Lafayette clays. Ba-rich feldspars have been observed by *Hewins et al.* [2013] in NWA 7533, a pair to the NWA 7034 Martian breccia [*Agee et al.*, 2013]. Li concentrations in Mars meteorites, both whole rock and in pyroxene grains, are <10 ppm [e.g., *Beck et al.*, 2004, 2006; *Barrat et al.*, 2002; *Herd et al.*, 2005; *Lentz et al.*, 2001].

1.5. LIBS Background

[9] LIBS is an emission spectroscopy technique in which a high-powered laser is focused on a solid, liquid, or gas and a portion of the material is converted to a plasma, exciting each species to a higher state. As the species relax, they emit at wavelengths characteristic of certain elements [e.g., *Cremers and Radziemski*, 2006]. This technique has developed rapidly over the last several decades and numerous experimental designs have been constructed tailored to meet specific needs. The hardware chosen (i.e., the lasers and spectrometers) and operational needs (i.e., standoff distance, energy density, and observational window of the plasma) constrain the obtainable accuracy and precision of a measurement. ChemCam was designed as a semiquantitative technique; so far it lacks the accuracy of a contact instrument like APXS, but in exchange, it provides a much larger number of analyses at high spatial resolution (~350 μm) for which approximate abundances can be obtained.

[10] For most elements, there are many emission lines and, if the plasma is optically thin, there is generally a linear relationship between each peak's intensity and the element concentration. In an optically thick plasma, e.g., a plasma with a very high density, it is possible for a phenomenon called self-absorption to occur. In this process, outer layers of plasma can absorb photons emitted by the central portion of the plasma, and under extreme conditions, an emission line may exhibit a characteristic peak shape with a dip in the center where the strongest absorption occurs. Under less extreme conditions, the peak area no longer increases linearly with concentration and the curve may be better fit with a second-order polynomial, exponential, or logarithm. According to *Bulajic et al.* [2002], intense peaks can begin to suffer from self-absorption at concentrations as low as 0.1 wt %, although the low pressure on Mars may reduce self-absorption. Use of calibration curves for univariate peak area quantification will take this nonlinearity into account; linear-based multivariate regression techniques such as partial least squares (PLS) may not be significantly affected if the nonlinearities are present in the set of spectra used in modeling and if such nonlinearities affect only a few peaks.

1.6. Previous Studies on Trace Elements Using LIBS

[11] Li has not been the subject of many LIBS studies. *Fabre et al.* [2002] developed a univariate calibration curve using the Li 670.7 nm unresolved doublet in several minerals. Under their operating parameters, they observed a linear relationship up to 0.3% Li and a second linear relationship from 0.3 wt % to the highest Li sample at ~8.5 wt %. *Wiens et al.* [2013] determined the limits of detection (LOD) for Li to be

between 0.3 and 25 ppm depending on the LOD metric for one set of ChemCam operating conditions.

[12] Ba concentrations in soils were calibrated using a univariate approach with the Ba 455.5, 493.4, and 553.55 nm emission lines and multivariate regression [*Essington et al.*, 2009]. The 493.4 nm line has the highest correlation with Ba content and the lowest relative error of prediction. They also investigated the effect of normalizing to the total spectral emission or to the Si 288 nm peak and found that normalizing to Si produces a better model. The Ba 233.5 nm line was used by *Eppler et al.* [1996] to develop univariate calibration curves in doped sand and soil matrices and found a linear correlation up to the highest concentration presented, 12,000 ppm Ba. *Lazic et al.* [2001] used the 553.55 nm Ba line and observed a highly nonlinear relationship up to 800 ppm Ba. The calculated LOD for one set of ChemCam operating conditions was determined by *Wiens et al.* [2013] to be between 46 and 973 ppm depending on the LOD metric.

[13] There are few studies on the use of LIBS to detect Rb in geological matrices. *Cousin et al.* [2011] list several Rb lines detectable under ChemCam-like operating parameters on geological materials but did not investigate Rb further. *Wiens et al.* [2013] discussed locations of Rb lines and overlapping peaks and calculated the LOD to be between 11 and 42 ppm depending on the selected LOD metric for one set of ChemCam operating conditions.

[14] Several LIBS studies have quantified Sr in solid nonbiological materials. *Mansoori et al.* [2011] analyzed cement powder and used the Sr II emission line at 407.77 nm and found a limit of detection of 20.3 ppm Sr. They built a univariate calibration curve using the ratio of the Sr line to a Ca line. Their experiment setup was nearly in situ (f = 35 mm) with 37 mJ/pulse energy, gated to optimize each element studied. *Martin et al.* [2012] used an in situ gated system with 50 mJ/pulse on $CaCO_3$ pellets doped with Sr as an analogue for nuclear fission products. They used the 460.8 nm Sr I emission line for univariate calibration and the full spectrum for multivariate analysis and found a detection limit of 10 ppm. *Fabre et al.* [2011] demonstrated the utility of the synthesized glass calibration targets that are attached to the *Curiosity* rover's body and periodically analyzed by ChemCam on Mars to quantify Sr. They used the data collected from the ChemCam flight model, which are also used in this study as test sets, to develop a univariate calibration curve using the Sr II 421.7 nm peak. *Wiens et al.* [2013] found the LOD to be between 15 and 358 ppm depending on the selected LOD metric for one set of ChemCam operating conditions.

2. Experimental Methods

2.1. Calibration Set

[15] Samples selected for the primary ChemCam calibration endeavor were chosen to encompass the expected range of the elements most likely to be encountered on Mars. Samples used in this analysis are listed with relevant compositional information in Table 1. Readers are directed to the publication by *Wiens et al.* [2013], which discusses the sample suite in detail. Eight of the samples are calibration targets (ChemCam Calibration Targets or CCCTs) that are replicates of materials sent to Mars on the rover [*Fabre et al.*, 2011; *Vaniman et al.*, 2012]. These targets are fabricated glasses (designated Picrite, Shergottite, and Norite due to their

Table 1. Trace Element Compositions of Standards Used in This Study[a]

Sample	Li (ppm)	Ba (ppm)	Sr (ppm)	Rb (ppm)
AGV2[c]	11	1130	661	66.3
BCR2	9	677	340	46.9
BEN[c]	13	1025	1370	47
BHVO2[c]	4.8	131	396	*9.11*
BIR1[c]	3.2	7.14	109	*0.2*
BK2[c]	-	1001	487	132
BT2[c]	-	480	559	-
BWQC1	-	122	161	26.1
Cadillac	-	711	49	129
GBW07104	18.3	1020	790	38
GBW07105[c]	9.5	498	1100	40
GBW07108	20	120	913[b]	32
GBW07110	17.5	1053	318	183
GBW07113	12.7	506	43	213
GBW07313	60	4400	267	97.3
GBW07316	35	2500	667	50
Granodike	-	212	264	*21.5*
GSR2	18.3	1020	790	37.6
GUWGNA	<u>2276</u>	51	-	<u>2020</u>
GYPA	-	*28*	930[b]	*1*
GYPB	-	*22*	118[b]	*1.5*
GYPC	-	*53*	296[b]	*<u>8</u>*
GYPD	-	*107*	152[b]	*<u>24</u>*
JA1	10.2	303	264	*10.7*
JA2[c]	29.1	315	250	71
JA3[c]	14	318	294	36
JB2[c]	7.78	208	178	*6.2*
JB3[c]	7.21	251	395	*13*
JDO1[c]	<u>0.4</u>	*6.14*	119[b]	*1.5*
JR1	<u>62.3</u>	*40*	30	257
KGa-Med-S[c]	<u>7433</u>	140	152	*6*
M6-Haggerty	-	1909	1282	68.5
Macusanite	<u>3528</u>	1.3	1.3	-
MHC1356	-	294	*51.3*[b]	*3.2*
MHC2319[c]	-	455	1931[b]	*1.3*
MHC3828	-	*78.5*	2053[b]	*22.2*
MO7	5.4	7480	1745	12
MO12	9.2	311	865	16
MO14	7.5	172	468	*4*
Moppin	-	273	405	17.4
MSHA	-	367	483	31.1
NAu2-Hi-S[c]	<u>7433</u>	56	*144*	*4*
NAu2-Lo-S[c]	<u>7433</u>	162	236	*9*
NAu2-Med-S[c]	<u>7433</u>	107	185	*6*
Norite[c]	44	355	284	-
Picrite[c]	7.2	1283	1481	-
SARM51	-	335	44	37
SGR1[c]	147	290	420	83
Shergottite[c]	7.5	1158	654	-
SRM688[c]	-	200	169	*1.91*
SRM88B	-	-	64[b]	-
SRM97A	510	670	1500[b]	-
SRM98A	325	270	330[b]	-
STSD1	11	630	170	30
STSD3	23	1490	230	68
STSD4	14	2000	350	39
Trond	-	347	668	21.8
Ultramafic[c]	-	*434*	<u>*283*</u>	35.8
UMPH	-	2980	<u>382</u>	74.1
UNSAK	-	-	2800[b]	-
UNSZK	279	-	-	860
VH1	-	277	50	<u>223</u>
VH49	-	37	234	*4.6*
VZO106	-	482	120[b]	35.1
VZO114	-	63	160[b]	10
WM	-	351	400	*3.7*

compositional similarity to picritic, shergottitic, and noritic materials), ceramics (NAU2-Lo-S, NAU2-Med-S, NAU2-Hi-S, and KGA-Med-S) designed to mimic expected compositions on Mars, and Macusanite, a natural peraluminous obsidian glass. All other samples are powdered (generally <60 µm grain size [*Wiens et al.*, 2013]) and homogenized pressed pellets that were used to eliminate grain size as a factor and minimize heterogeneity. Samples were obtained from a variety of sources including Brammer's Standard Company, Inc., the United States Geologic Survey (USGS), the National Institute of Standards and Technology (NIST), the Clay Minerals Society (CMS), and the collection of M. D. Dyar at Mount Holyoke College.

2.2. Instrument Description and Data Collection

[16] The ChemCam LIBS uses a Nd:KGW (neodymium-doped potassium gadolinium tungstate) pulsed laser providing up to 14 mJ on target at 1067 nm to generate a small plasma on a target. Plasma light is collected and transmitted through a telescope to an optical fiber and demultiplexer that splits the light to three spectrometers: ultraviolet (UV; 240.0–342.2 nm), violet (VIO; 382.1–469.3 nm), and visible to near-infrared (VNIR; 473.7–906.5) [*Maurice et al.*, 2012; *Wiens et al.*, 2012]. The full width at half maximum (FWHM) for each spectrometer is 0.15 nm, 0.20 nm, and 0.65 nm for the UV, VIO, and VNIR, respectively. Data used for this study were obtained during calibration of the ChemCam flight model (FM) at the Los Alamos National Laboratory, Los Alamos, New Mexico. Two calibration data sets were collected (Table 2): one with the FM at room temperature (20°C) referred to here as the room temperature calibration (RTC) and the other with the FM in a thermal vacuum chamber (TVAC) with the laser at −10°C. The RTC was conducted at 3 m with an approximate laser output of 9.5 mJ per 5 ns pulse. The TVAC tests were conducted at 1.6, 3, 5, and 7 m with a laser output of 10 mJ per pulse at 1.6 m and 14 mJ per pulse at the other distances. Forty (RTC) or 50 (TVAC) spectra were taken at four locations on each sample. The laser was operated at 3 Hz (nominal ChemCam repetition rate) for all tests. During analysis, samples were housed in a chamber containing a 7 Torr CO_2 atmosphere to approximate expected conditions on Mars.

2.3. Spectral Pretreatment

[17] An ambient light background spectrum obtained on the sample without firing the laser is subtracted to remove non-LIBS signal. Spectra are then denoised using a wavelet transform method, the continuum is removed, and the instrument response function is applied. Details of this procedure are described in *Wiens et al.* [2013]. Peak areas are obtained

Notes to Table 1

[a]Underlined values indicate those samples were not used in modeling for the particular element. Hyphens indicate no chemical information is available. Samples in bold are calibration targets that are on the Mars rover. Macusanite was not shot for any database but spectra taken while on Mars are available. Values in italics indicate that sample's peak was not fit for univariate modeling but the samples were used for PLS.
[b]Samples removed for matrix-matched modeling.
[c]Samples shot at multiple distances during TVAC calibration. MHC2319, Norite, Picrite, SRM688, and Ultramafic were only shot at 1.6 and 3 m; shergottite was shot at 1.6 and 3 m but 3 m data were unavailable. STSD1 was also shot a multiple distances but TVAC data for this sample were excluded due to missing data.

Table 2. Experimental Data Sets

Description	Distance (m)	Output Energy (A, mJ)	On-target Energy (mJ)[a]	Spot Size (μm)[b]	Fluence (J/cm²)
RTC[c]	3	95, 9.5	9	207	21
TVAC[d]	1.6	60, 10	8	183	24
TVAC	3	95, 14	11	207	26
TVAC	5	95, 14	11	242	19
TVAC	7	95, 14	11	276	14
CCCTs[e]	1.6	40-60, 6-10	6-10	181	18-31

[a]Laser output reduced by 8% for the RTC and 20% for the TVAC due to mirrors and windows.
[b]Radius from *Maurice et al.* [2012].
[c]Room temperature calibration; laser at 20°C.
[d]Thermal vacuum calibration; laser at −10°C.
[e]Data used from sol 27, sol 49, sol 66, sol 75, sol 76, sol 134, sol 153, and sol 192.

directly from these data; normalization to the total emission for the appropriate individual spectra range (UV, VIO, or VNIR) is done to the obtained peak area. Multivariate modeling is done using spectra that have been normalized to the total emission by spectral range. Normalization is a common procedure in LIBS data processing that is used to correct for systematic effects such as variations in laser intensity. This procedure can be done in a variety of ways and in this situation we have chosen to normalize to the total emission by spectral range. By normalizing to the individual spectral range, anomalies with the instrument response function, hot pixels, spikes in emission due to cosmic rays striking the detectors, etc., are not distributed to the entire spectrum.

[18] A visual inspection of the spectra revealed that up to the first five shots at each analysis spot often had surface contamination in the form of adsorbed water and/or manipulation residues. Previous studies using these data have simply removed the first five spectra; in this study, we chose to use an outlier removal algorithm based on the Pearson's correlation coefficient described in *Oldham et al.* [2008]. This algorithm typically removed 3 to 10 spectra from the group of 160 spectra, and 65% of the removed spectra are among the first five shots. After this removal process, the remaining spectra were evenly distributed into three groups with 45 spectra in each. Each group of 45 was then averaged to form a single spectrum, resulting in three spectra for each target. This homogenization of the spectra was deemed necessary for the trace elements which, due to their low signal, are more susceptible to slight compositional and/or laser intensity variations across the four locations on each pellet. Therefore, the LIBS signal should more closely represent the reference composition.

2.4. APXS Calibration

[19] When taken on the same target, APXS data for major and trace elements are compared to ChemCam estimates. A brief description of the APXS technique is described below and readers are referred to the listed citations as well as *Schmidt et al.* [2013] for additional details.

[20] The APXS employs two well-known methods of X-ray emission analysis simultaneously. Its six ^{244}Cm sources decay primarily by alpha particle emission, and 90% of these decays give rise to subsequent emission of the L X-rays of the plutonium daughter atom. At the sample, the alpha particles cause particle-induced X-ray emission (PIXE), while the Pu L X-rays cause X-ray fluorescence (XRF). PIXE preferentially

excites the lighter elements from Na upward, with the excitation probability declining rapidly with increasing atomic number Z [e.g., *Johansson and Campbell*, 1988]. XRF preferentially excites the heavier elements, but its contribution declines with decreasing Z [e.g., *Van Grieken and Markowicz*, 1993]. Thus for Ti, the two excitation modes contribute about equally but as Z increases, the XRF:PIXE ratio for Fe reaches ~95%. The two modes are thus well balanced and provide a conveniently uniform sensitivity for Na-Sr.

[21] To convert these dual-technique spectra to element concentrations, a software package GUAPX was developed by *Campbell et al.* [2009, 2010]. This combines a nonlinear least squares fit of the spectrum with a rigorous treatment of matrix absorption effects based on the fundamental physics of XRF and PIXE. GUAPX is a derivative of the widely used PIXE software code GUPIX [*Maxwell et al.*, 1995]. During the final refinement of GUAPX, spectra from the geochemical reference materials used in the MER APXS calibration of *Gellert et al.* [2006] provided valuable input for testing.

[22] The MSL APXS was calibrated using an expanded suite of ~60 geochemical reference materials, including a greatly increased contribution of sediments [*Campbell et al.*, 2012]. The GUAPX results were presented in the form of ratios (R-value) between the GUAPX concentration and the certified concentration for each element. For most elements, the mean R-value across the standard was close to unity, with a scatter attributable to counting statistics, peak fitting error, and sample heterogeneity. The latter term simply reflects the fact that certain elements are hosted mainly by certain minerals and not by others. For certain elements in certain rock types, e.g., Al and Mg in basalts, departures from unity up to ~20% are observed. If the mineralogy is known, empirical corrections can be applied to refine such results.

3. Statistical Methods

[23] There are two categories of techniques commonly used to develop calibration models, univariate and multivariate techniques. Univariate models often consist of fitting a linear regression model to data from a dilution series in which the target element concentration is progressively decreased within a controlled matrix [e.g., *Hilbk-Kortenbruck et al.*, 2001]. This is a useful technique for LIBS data as it has been shown that emission lines can be significantly affected by the matrix, either the chemical matrix or the physical matrix [*Eppler et al.*, 1996; *Krasniker et al.*, 2001; *Anzano et al.*, 2006; *Bousquet et al.*, 2007]. But development of matrix-matched calibration curves for every element for every geological matrix would be impractical and in most of the analyses presented here, all samples regardless of the chemical matrix are used. The physical matrix is controlled by powdering and pressing the samples into pellets. Development of matrix-matched models for targeted matrices may improve results and will likely be used on a case-by-case basis as new data are received from Mars.

[24] To mitigate the influence of matrix effects and reduce the reliance on a single peak for modeling, researchers have applied multivariate statistical techniques to LIBS spectra of geological materials [e.g., *Laville et al.*, 2007; *Clegg et al.*, 2009; *Tucker et al.*, 2010; *Dyar et al.*, 2010, 2012; *Anderson et al.*, 2011, 2012; *Lasue et al.*, 2012]. PLS has

been used by the ChemCam team for rapid major element abundance determination [*Wiens et al.*, 2013]. However, PLS is often less viable in its current form for minor and trace elements due to their relatively small signals and/or low abundances. Moreover, PLS tends to predict minor element abundances based strongly on major element emission lines due to geochemical isomorphous substitutions, such as that of Rb^+ for K^+ in feldspars [*Speicher et al.*, 2011]. Univariate modeling may therefore be required for trace elements, even though the results are known to be affected by matrix effects. Training sets for both univariate and PLS modeling are obtained from the RTC data set, which contains the most extensive suite of samples, and these models are tested using the TVAC data sets, which contain a more limited selection of samples, as well as the nine CCCTs.

[25] For most of the trace elements, the training set does not have standards with an even distribution across the relevant composition ranges expected to be encountered on Mars. Often the upper compositional ranges are underrepresented in the training sets. This uneven distribution generally results in a lower error estimate than would be obtained if the lower concentration range were reduced to match the upper concentration range. However, if there are no significant outliers present that may be incidentally removed in an attempt to balance the compositional range, estimates will not change significantly and therefore, for this preliminary study, no attempts were made to balance the compositional range. It is expected that these results will be reevaluated when a more complete training set has been developed.

3.1. Univariate Modeling

[26] For each trace element studied here, a generalized sequential series of modeling techniques was applied. Univariate models were built using peak areas from all peaks large enough to fit using one emission line per element. The PeakFit 4.12 commercial software (Systat Software, Inc.) was used to set a local linear background over a small range around the target peak and the peak is fit either with a Gaussian or Voigt profile; details on these procedures will be described in the appropriate section for each element. Least squares regression models were built using the program "lmcal" in the "quantchem" package [*Komsta*, 2012] from the open source software R [*R Development Core Team*, n.d]. Univariate models are cross-validated using a "leave one sample out (three spectra per sample)" method and the removed spectra are predicted in the model. These predictions are then used to determine the root-mean-square-error of prediction (RMSEP) for comparison to the PLS models, as described in the following sections. The "quantchem" package was used to quickly build multiple models for the cross validation.

3.2. Multivariate PLS Modeling

[27] Briefly, PLS regression produces a calibration model by projecting the data into a new dimensional space and regressing two data matrices, *X* and *Y*, against each other [e.g., *Naes et al.*, 2004]. The *X* matrix, or the input matrix, consists of the set of spectra or the selected wavelength ranges from the spectra. The *Y* matrix consists of the element compositions or the set of compositions. If a set of compositions of more than the element in question is used, the technique is referred to as PLS2, and the modeling will reduce the covariance between the linear functions for both matrices.

Often, not all trace elements are analyzed for geochemical reference materials. Thus, the training set must be customized for each element separately to include only reference materials with valid compositions for the element of interest. This precludes the PLS2 method, which builds a model to predict multiple elements at once. Therefore, for this study, each element is modeled individually (PLS1). The PLS modeling produces linear combinations of the *X* matrix that describes the variance between the *X* and *Y* matrices; these are called components or latent variables (LVs). Selection of the appropriate number of LVs is of primary importance for building robust models and the choice of LV can be made using the RMSEP (described below).

[28] In this study, one or more PLS models were constructed using the "plsr" package [*Mevik and Wehrens*, 2007] in R for comparison to the univariate models. The "plsr" package automatically mean-centers the data matrix. PLS models are cross-validated using the same "leave one sample (three spectra per sample) out" method used in the univariate modeling cross-validation. Multiple PLS models were built to optimize the analysis of the particular element. Initially, a model using nearly the entire spectral range (246.5–335.7, 388–469, and 492.5–857 nm) was built to establish a baseline. This model is expected to have the highest error and be the least robust due to influence from the many other peaks in the spectra, some of which are correlated to the trace element in question due to the geochemical affinities between major and trace elements, mentioned previously. The second PLS model mean-centers and standardizes the matrices to a standard deviation of one. Standardizing the wavelength bins equalizes the variables and so large peaks no longer have more influence than small peaks, thus increasing the contribution of trace elements to the modeling. The final PLS model is developed on a reduced wavelength range selected to have a high (>0.6) Pearson's correlation coefficient between the wavelength and the element. Due to strong correlations between elements, these select wavelengths are further reduced to only those known to correspond to an emission line of that element. This model should produce similar results to a univariate model but does not require peaks to be fit.

3.3. Error Analysis and Component Selection

[29] To allow comparisons between univariate models and PLS models, we have chosen to use the RMSEP for the error assessment for all modeling. RMSEP is a measure of the variability between predicted and reference values for the sample training set. The RMSEP is calculated as the square root of the sum of the square of the differences for the *i*th value (d_i) between a reference value (r_i) and a predicted value (p_i) ($d_i = r_i - p_i$) divided by the number of data points (*n*):

$$\text{RMSEP} = \sqrt{\left(\sum (d_i)^2 / n\right)}$$

[30] For PLS modeling, the RMSEP can be used to select the appropriate LV, previously described as key to making accurate estimates. The choice of LV is critical to building a model that is sensitive enough to be able to accurately predict a sample's composition while not reaching the point where the noise becomes a factor or the model becomes too specific to the training set. A robust model is particularly

Table 3. Spectroscopic Data of Emission Lines Used in Modeling

Species	λ (vacuum, nm)	$E_i - E_k{}^a$ (eV)	No. of Channels (Selected λ for PLS)	Average Correlation Coefficient
Rb I	303.28/303.30	0.0–4.1	5 (303.36–303.56)	0.79
Rb I	780.24	0.0–1.6	5 (779.85–780.67)	0.89
Sr II	407.89	0.0–3.0	5 (407.77–407.94)	0.66
Sr II	421.67	0.0–2.9	15 (421.28–421.90)	0.70
Sr I	460.86	0.0–2.7	7 (460.76–460.99)	0.63
Li I	670.96/670.98	0.0–1.8	15 (668.63–671.62)	0.89
Li I	812.85/812.87	1.8–3.4	6 (812.52–813.53)	0.91
Ba II	455.53	0.0–2.7	16 (455.39–455.97)	0.75
Ba II	493.55	0.0–2.5	5 (493.10–494.01)	0.84
Ba II	614.34	0.7–2.7	3 (614.05–614.49)	0.67
Ba I	650.06	1.2–3.1	2 (649.97–650.18)	0.62
Ba I	728.23	1.1–2.8	4 (727.72–728.35)	0.69

[a]Obtained from *Kramida et al.* [2012].

important when the operational system has as many variables as ChemCam does. Analyses on Mars are done at different distances, laser energies, material types (soils/rocks), surface textures, and incidence angles. These factors will inevitably reduce the accuracy of the analyses, but a robust model will be as generalizable as possible. Commonly the LV associated with the first local minimum RMSEP or the global minimum RMSEP over a set number of components, e.g. 20 LVs, is chosen.

[31] However, ChemCam's current situation requires a unique set of criteria to be established to select the optimal LV. At the present time, the RTC data set is the only data set with a sufficient number of samples of a variety of chemical matrices to be able to model on and is representative of a single operating condition (Table 2). ChemCam will generally operate at a higher energy than was obtained under any of the training sets, including the TVAC data sets. ChemCam will also operate at distances up to 7 m, as represented by the TVAC 1.6, 3, 5 and 7 m data sets. A distance correction algorithm is in development [*Mezzacappa et al.*, 2013] but was unavailable for use in this study. In addition to the energy and distance, which can be considered together under the umbrella of on-target fluence, there is the additional issue of differences between spectra taken on Earth in a Mars chamber and Mars itself. These effects can be studied to a certain extent using the CCCTs, which were analyzed on Earth at the same distance as they are analyzed on Mars (1.6 m) and the same energy output (60 A on Earth, 40–60 A on Mars). The on-target fluence (Table 2) is 24 J/cm^2 on Earth and 18 to 31 J/cm^2 on Mars. Differences between simulated Mars and actual Mars include gas composition (100% CO_2 versus 96% CO_2, 1.9% Ar, 1.9% N_2, and trace O_2 and CO [*Mahaffy et al.*, 2013]), pressure (7 Torr versus 5.6 to 6.2 Torr, converted from *Haberle et al.* [2013]), and atmospheric density. Notable differences between spectra include increases in C and O peak sizes on Mars. The listed factors are currently being investigated to determine if these differences significantly affect calibration results. It may be that new training set spectra will be required to encompass these sources of variability.

[32] Until such a training set is available, additional steps are required to ensure that the optimal LV is being used for all operating conditions since the optimal LV for the training set may not be acceptable at different distances or for Mars data analysis. First, we build a model using the RTC training set as previously described and the RMSEPs from the validation for LVs 1–20 are tabulated. Data from the TVAC data

sets and the Mars CCCTs are then predicted in the model and the first 20 LVs for these data sets are calculated and all RMSEPs are combined in a table and the sum of the RMSEPs for each LV is determined. The goal is to minimize the RMSEP across all data sets but more emphasis is placed on the training set, TVAC 1.6 and 3 m, and CCCTs on Mars because ChemCam most often operates at distances of < 4 m. During this process, it was noted that simply selecting the lowest RMSEPs does not necessarily indicate the model is acceptable as there may be little correlation between the actual composition and the predicted composition, particularly if the compositional range of the data set is highly skewed toward the lower concentration range. It was decided that it was more important to approximately characterize high-abundance samples than to obtain high accuracy for the low compositions. As a quick check, plots of reference composition versus predicted composition were made for each data set for each of the 20 LVs and these were qualitatively evaluated prior to the selection of the RMSEP to be sure this aim is met.

[33] Next, the best model is tested on Mars data. One such test is to see how the model's estimates behave for shot-to-shot data. When interrogating a point on a rock, single-shot abundance estimates should be fairly consistent as the peaks generally do not vary significantly over the small depth profile or, if there is a significant change in composition, the estimates should change relatively smoothly. Examination of the shot-to-shot estimates for Mars targets indicates consistency up to 15+ LVs for PLS models that incorporate a large wavelength range. However, for the reduced wavelength range model (recall it is essentially a univariate model), after more than a few LVs, in general, the shot-to-shot estimates begin to vary widely. This is expected given there are few wavelength variables remaining in the model and therefore the "noise," which in this case corresponds to differences in continuum removal that appear at the edges of the peaks and additional influence from the less important peaks, begins to quickly degrade the predictive capability of the model. To test whether the selected LV has an acceptable level of shot-to-shot precision, estimates for LVs 1–20 are examined. A qualitative assessment is made to quickly reduce the number of selectable components to those that have relatively smooth shot-to-shot estimates. After all of these factors are considered, the number of LVs is selected and the chosen model is used to obtain compositions of the Mars targets.
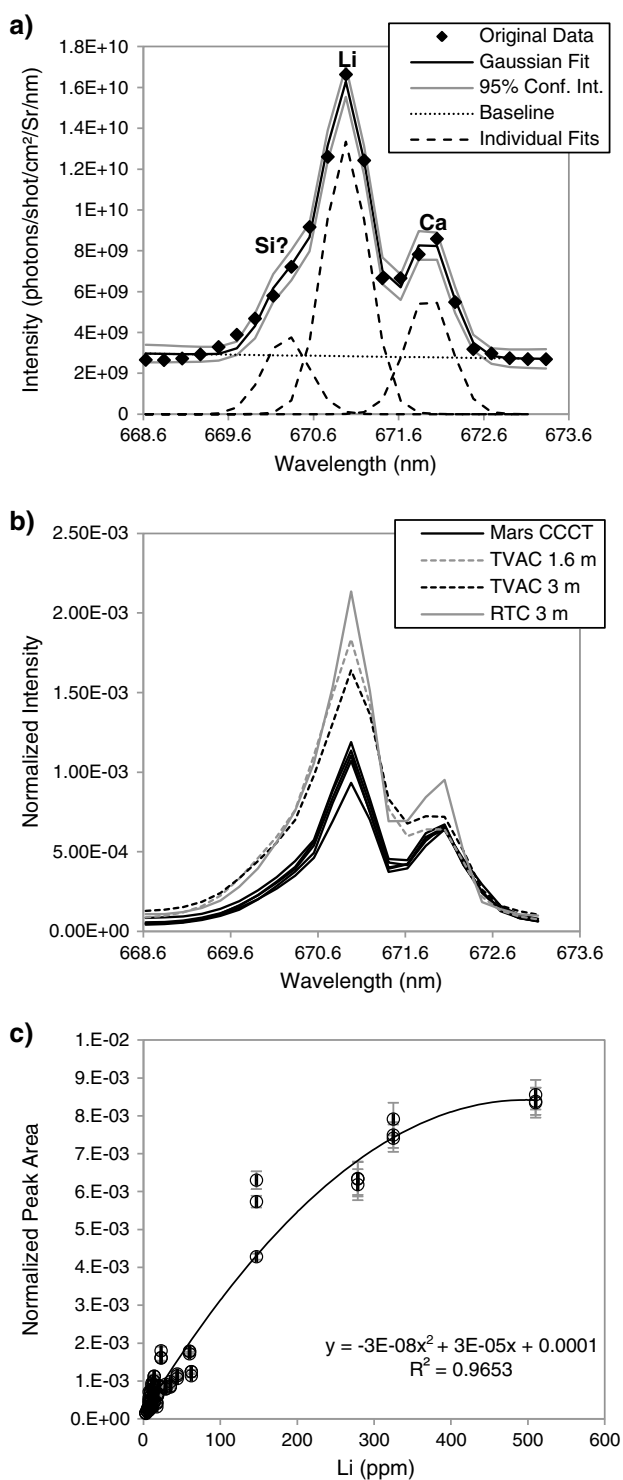
Figure 1. (a) Example Gaussian fit for the Li 671 nm peak on the RTC spectrum for Norite. (b) Comparison of Norite spectra taken on Mars (CCCT), TVAC 1.6 and 3 m, and the RTC. (c) Univariate peak area model for Li.

4. Calibration Models

4.1. Lithium

[34] The full available compositional range for Li includes the ceramic calibration targets (7433 ppm Li) and GUWGNA (2276 ppm Li); the next highest Li concentration is 510 ppm

(SRM97A). There are three standards with Li between 510 ppm and 147 ppm, and there are 28 standards with less than 62 ppm Li. This study uses only standards with 510 ppm or less.

[35] The primary Li peak is an unresolved doublet at 670.96/670.98 nm (Table 3), a secondary Li peak is an unresolved doublet at 812.85/812.87 nm, and a third unresolved doublet is at 610.52/610.52 nm. The primary Li line is present at concentrations down to the lowest available in the training set, BIR with 3.2 ppm. The secondary Li line is generally present at higher concentrations ($> \sim 20$ ppm) and it is on the edge of a large Na peak at 818.55 nm, which may obscure the presence of Li at this location. The third peak overlaps significantly with a Ca peak at 610.44 nm and is not used in this study.

[36] The univariate model (U1) was constructed by fitting a Gaussian profile to the Li I 671 peak for all 32 standards available. Figure 1a shows an example fit for one of the Norite CCCT spectra from the RTC data set and Figure 1b compares the Norite CCCT between the various data set; note TVAC 5 and 7 m are not available for Norite due to poor coupling between the laser and sample at these distances. Figure 1b hints at a potential problem with estimating Li. After normalization, the spectra taken on Mars show the Li peak at $\sim 1/2$ the height of the RTC spectra on which the model is built. There are no other CCCTs with an appropriate range to test if this is an anomaly with Norite alone or if it will be a systematic difference with Li on Mars. Picrite and Shergottite CCCTs have much lower Li abundances, ~ 7 ppm, and the Picrite Li peaks are significantly smaller in amplitude on Mars while Shergottite Li peaks are of similar size between Earth and Mars. Macusanite and the ceramic CCCTs have high Li concentrations (3528 ppm and 7433 ppm, respectively) and therefore these samples are beyond the range of the model. However, normalized peak areas between Earth and Mars for the ceramic CCCTs are of similar size, indicating the issue may be with the Norite target or a matrix effect. Given the currently available information, we cannot say if there will be a systematic underestimation of Li, but we note the possibility.

[37] The univariate concentration versus peak area model for Li is shown in Figure 1c. Error bars are from the PeakFit software and represent the standard error for the entire fit, including the baseline. The data were best fit with a second-order polynomial, indicating self-absorption is occurring in the plasma. The highest concentration sample was unable to be predicted in the polynomial regression model due to the square root term being an imaginary number. For these three spectra, a separate linear regression model was used to predict them. The resulting RMSEP is 36 ppm. Figure 2a is a reference versus predicted concentration plot which shows that 36 ppm is likely an underestimate on the error due to the higher density of samples < 60 ppm. Examination of the TVAC and CCCT estimates in Figures 2b–2f show that there is the potential for over- or under-estimates at higher concentrations (~ 150 ppm), but in most cases a "high" concentration can be distinguished from a "low" concentration. The univariate modeling is consistently at or below a RMSEP of ~ 55 ppm and the training set RMSEP is 36 ppm.

[38] Three PLS models were constructed and examined. Model P1 uses the full wavelength range, and examination of the RMSEPs for the first 20 LVs and the reference versus predicted plots indicates that seven LVs are optimal for this
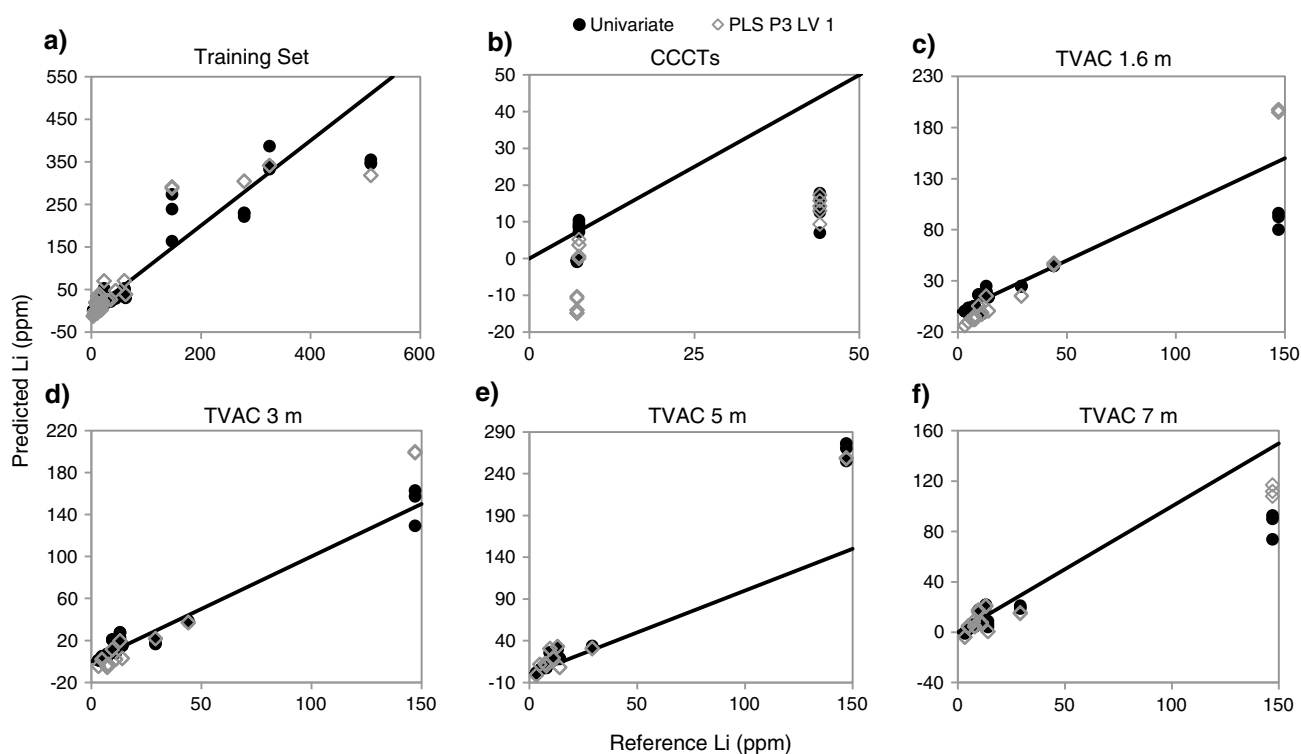
Figure 2. Reference versus predicted composition plots of Li univariate and PLS models for the (a) RTC training set, (b) the CCCTs, (c) TVAC 1.6 m (d) TVAC 3 m, (e) TVAC 5 m and (f) TVAC 7 m data sets. Lines indicate 1:1 composition estimates.

model. LV 7 does not predict the high concentration standard (SGR1 147 ppm) well for the TVAC data but it is acceptable for the training set and CCCTs. The RMSEP for the training set for this model is 45 ppm and the sum of the RMSEPs for each data set is slightly higher than the univariate model.

[39] Model P2 uses the full wavelength range but standardizes each wavelength bin. Unlike P1, this model predicts the high concentration sample fairly well but the low concentration range is predicted very poorly in the TVAC data set, often predicting >50 ppm for samples with <15 ppm. The training set and CCCTs are also predicted poorly for all LVs; the optimal LV appears to be three.

[40] The final PLS model, P3, uses a wavelength range that has been reduced to 33 channels over the Li I 670 nm and Li I 813 nm peaks (Table 3). Based on the training and test sets, LV 11 would be the optimal choice as there is excellent discrimination between high and low concentration and good accuracy at both ends. However, this is a large number of LVs for a model with only 33 variables in the X matrix, and therefore additional information is needed to determine if this number of LVs provides stable estimates. Examination of the shot-to-shot estimates for an example Mars target, in this case Bathurst_Inlet, which has a relatively large Li peak, reveals that LV 11 is not the optimal choice (Figure 3). LV 11 has shot-to-shot estimates that can vary from 65 ppm to 10 ppm in a single shot while the LV 1 follows the Li 671 nm peak intensity closely. The RMSEP for LV 1 for the training set is 44 ppm and the sum of the RMSEPs for the data sets is the lowest of the PLS models discussed.

[41] RMSEPs for each data set are shown in Figure 4a. Examination of this figure indicates that the models with

the lowest errors are the univariate model and the PLS P3 model with 1 LV, which should be (and is) very similar to the univariate model. The averaged spectra for each analysis point on Mars (excluding the first five shots, which are typically the shots that show influence from dust), for each model are compared in Figure 5a. Overall, the two models are consistent and there is a cross-over point at around 20 ppm where PLS gives higher estimates above 20 ppm and lower
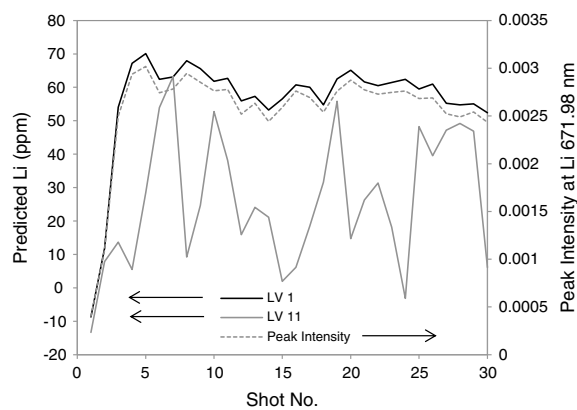

Figure 3. Single-shot PLS model P3 Li predictions on a 30 shot depth profile of Bathurst_Inlet for LV 1 and LV 11 compared to the Li 671 nm peak intensity. LV 11 shows significant fluctuations in Li estimates compared to LV 1. Predictions based on LV 1 closely follow peak intensity. Arrows indicate which axis is associated with which line.
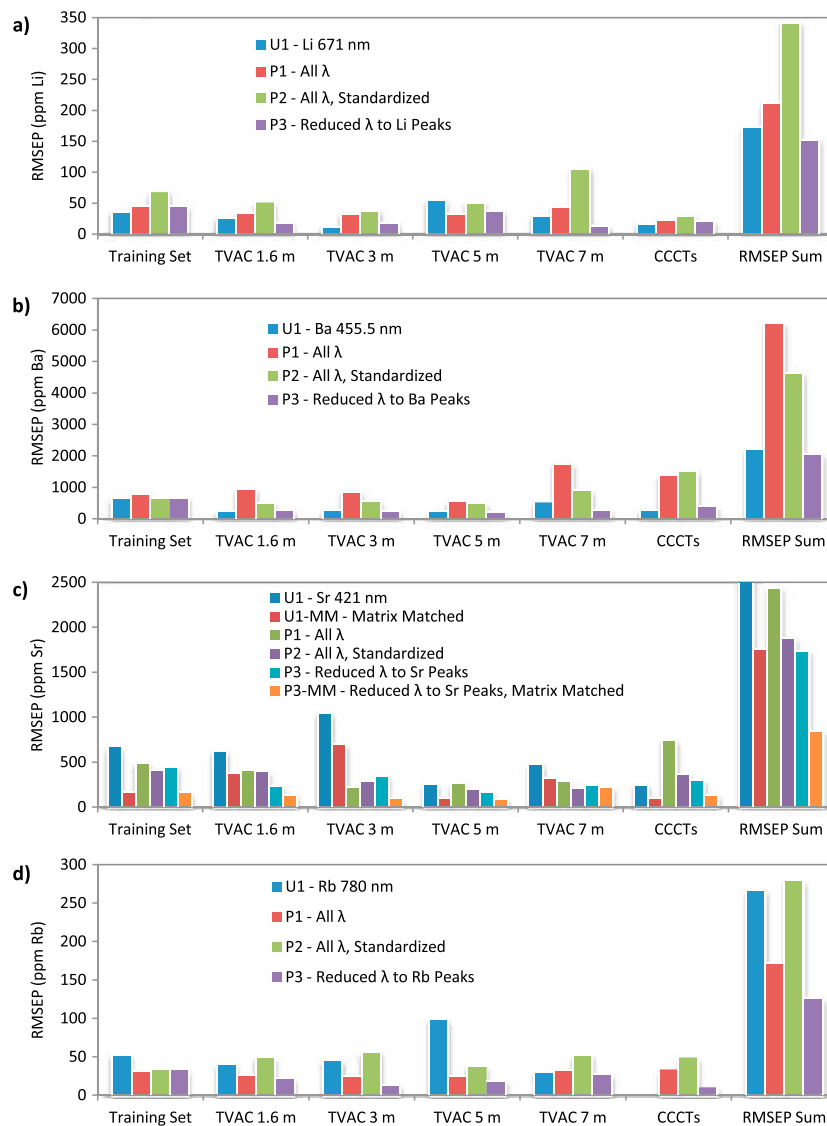
Figure 4. RMSEP for the RTC training set, CCCTs, TVAC 1.6 m, TVAC 3 m, TVAC 5 m, and TVAC 7 m data sets and the total RMSEP for (a) Li, (b) Ba, (c) Sr, and (d) Rb.

estimates below 20 ppm relative to the univariate model. Due to the lesser number of negative predictions in the univariate model, this model is preferable for final abundance estimates.

4.2. Barium

[42] The training set for Ba covers the concentration range from 7 to 7480 ppm. The suite of standards is heavily weighted toward the low concentration range with only 3 samples over 3000 ppm, 12 samples between 1000 and 3000 ppm, and 40 samples below 1000 ppm. There are five Ba lines in the ChemCam range that can be detected: Ba II 455.53 nm, Ba II 493.55 nm, Ba II 614.34 nm, Ba I 650.06 nm, and Ba I 728.23 nm (Table 3). The Ba 493.55 nm line is present in the training set at concentrations down to ~300 ppm. Ba 614.34 nm is located between two midsized Ca lines, and, in high Ca targets, the space between the lines rises upward, which may subsume the Ba peak. In the training set, this Ba peak is present down to concentrations of ~300 ppm and there is a slightly overlapping Fe line that is present in high Fe standards. The Ba 650.06 nm line forms a shoulder on a

small Ca peak and Ba 728.23 nm is the least sensitive Ba line, present only down to ~600 ppm.

[43] The most sensitive Ba emission line in the training set is the Ba 455.53 nm line and its presence can be detected down to ~100 ppm. This line is surrounded by three Ti lines and an unknown line that overlaps the second Ti line (Figure 6a). It is likely this unidentified line is Si III due to its presence in Macusanite, which is high in Si, although doubly ionized lines are rarely present in ChemCam spectra, nor are lines with such high excitation energies ($E_i = 19.01$, $E_k = 21.74$ eV [*Kramida et al.*, 2012]). However, no other transition listed in the NIST database fits with the emission line at ~455.49 nm in Macusanite. The presence of the putative Si line may be tied to the on-target laser fluence. In Figure 6a, the spectra of the CCCTs taken on Mars, which have higher on-target fluences than the RTC training set, show the presence of this line slightly in Picrite (top) and more prominently in KGa-Med-S (bottom). Comparing the Mars spectra for KGa-Med-S to the TVAC 1.6 and 3 m spectra, there are similarities in the region around the Si line
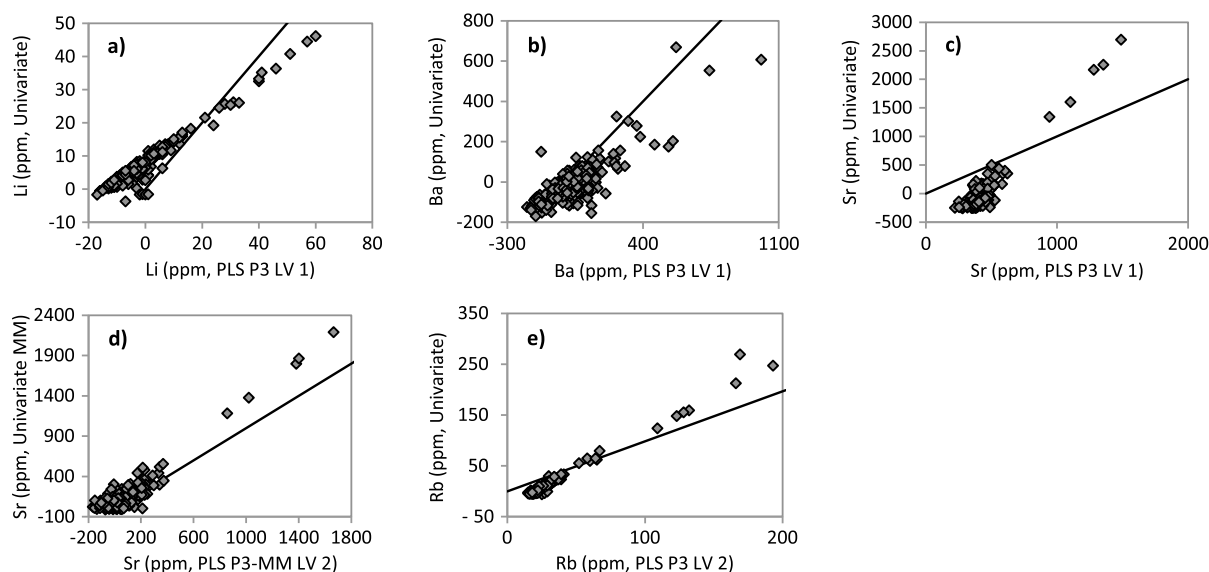
Figure 5. Comparison of selected univariate and PLS models estimates for all Martian targets for (a) Li, (b) Ba, (c) Sr, all samples, (d) Sr, igneous matrix-matched, and (e) Rb. Lines indicate 1:1 composition estimates.

while the TVAC 5 and 7 m data and the RTC do not show this pattern.

[44] In spite of these complications surrounding the 455.54 nm Ba emission line, it is still the best Ba peak for univariate modeling. Figure 6b provides examples of how these lines were fit with Voigt profiles. Given the close spacing between the peaks, fitting this region is difficult. The univariate model based on the training set peak fits are shown in Figure 6c. The data were fit with a second-order polynomial due to what appears to be a small amount of self-absorption past 4000 ppm. There is significant scatter at the mid to low concentration range (<3000 ppm) and this is likely due both to several potential outliers and the difficulty in fitting the Ba peak. The outliers will be investigated further but we have chosen to leave them in the model because they are evenly distributed around the regression line. Thus, they do not significantly influence the estimates but the RMSEP will be increased. The RMSEP on this model is 640 ppm; two spectra from the highest concentration standard (MO7) were unable to be predicted with the quadratic formula and were predicted with a linear regression model instead. Estimates for the training set, TVAC and CCCT data sets are shown in Figure 7. This plot will be discussed further after the PLS models have been described; however, we note that for the CCCTs, Macusanite, which has a Ba concentration of 1.3 ppm, was fit following the same peak locations and methods as the other standards and is overestimated by ~80 to 200 ppm. This indicates that the fitting procedures are not optimal when the putative Si peak dominates and care should be taken when interpreting data taken on similar spectra of unknown composition.

[45] Three PLS models were constructed for Ba. Model P1 uses the full wavelength range and the global minimum RMSEP over the first 20 LVs for the training set is at LV 20, indicating that the model may not have reached the true global minimum. The reference versus predicted composition plots indicate that there may be several outliers that are over-predicted and several that are under-predicted. Outside of these outliers, there is good discrimination between high

and low concentrations for LVs 15–20. The TVAC sets are not very well predicted for any LV, but 10 LVs appears to have the best balance between accuracy and high/low concentration discrimination. In the TVAC, MHC2319 (455 ppm) is overestimated by a factor of ~6, possibly due to its high Si content (68 wt %) as previously discussed in the univariate modeling section, and MHC2319 is one of the potentially serious outliers in the training set model. For the CCCTs, LV 2 is the optimal LV. Striking a balance between the optimum LV for the training set (LV 15–20), TVAC (LV 10), and the CCCTs (LV 2) is difficult, and placing more weight to the training set and TVAC 1.6 and 3 m sets gives a compromise LV of 15, which has an RMSEP of 764 ppm for the training set.

[46] The second PLS model, P2, uses the full wavelength range and standardizes and centers each wavelength across the matrix. The training set for this model is very similar to the previous model, and again the global minimum occurs at LV 20. Inspection of the RMSEPs and reference versus predicted plots for the TVAC and CCCT test sets shows that no LV has estimates that are accurate or very good at discriminating high concentrations from low concentrations. The one benefit from this model is that in the test sets, MHC2319 does not appear to be a significant outlier for most LVs. For this model, the LV associated with the global minimum RMSEP for the training set is chosen simply because no LV is any better or worse in the test sets. LV 20 has an RMSEP of 648 ppm for the training set.

[47] The final model, P3, uses 30 wavelength channels over five Ba peaks (Table 3). While the training set RMSEP is lowest at eight LVs, the model is acceptable across all 20 LVs. The TVAC and CCCT tests have low RMSEPs, good high/low discrimination for the first two LVs, and the shot-to-shot estimates for a Mars target that appears to have Ba (Preble 2) are consistent and track with the 455.5 peak intensity. Both LVs overestimate Macusanite, which, as previously discussed, is likely due to the putative Si peak located near Ba. Between LV 1 and LV 2, LV 1 is preferable because, for the TVAC distance test sets, JDO1
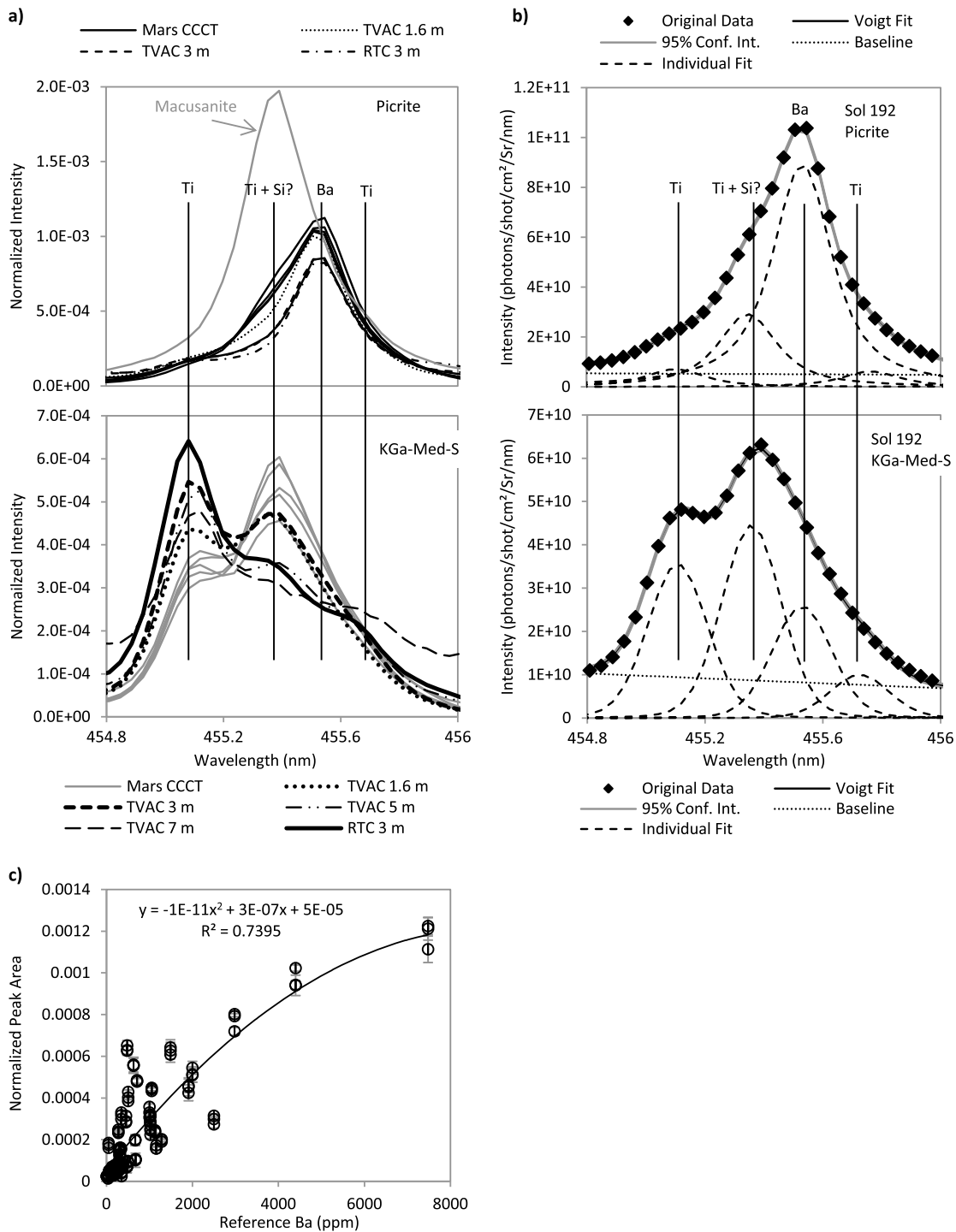
Figure 6. (a) Comparison of the Ba 455.53 nm region for the RTC, TVAC and CCCTs for Picrite (top, Ba: 1283 ppm, SiO_2: 44 wt %, TiO_2: 0.4 wt %) and KGa-Med-S (bottom, Ba: 140 ppm, SiO_2: 36 wt %, TiO_2: 1.5 wt %). The upper plot also has a spectrum from the Macusanite CCCT (Ba:1.3 ppm, SiO_2: 74 wt %, TiO_2: 0.04 wt %) to illustrate the position of the unidentified peak. (b) Example Voigt profile fits for a high Ba standard (Picrite, upper) and a high Ti/low Ba standard (KGa-Med-S, lower). (c) Univariate polynomial calibration curve for Ba.

(carbonate with 1.6 ppm Ba and low Si) is over-predicted, possibly due to interference from high Ca around the Ba 614 and 650 nm lines. Thus, selection of LV 1 may increase the robustness of the model in high Ca targets. The RMSEP for the training set is 670 nm for 1 LV.

[48] Between the RMSEPs of the three PLS models and the univariate model (Figure 4b), the univariate and PLS P3 models are approximately the same and both are considerably better than the two PLS models that use the full wavelength range. Comparison of the univariate and PLS P3 reference
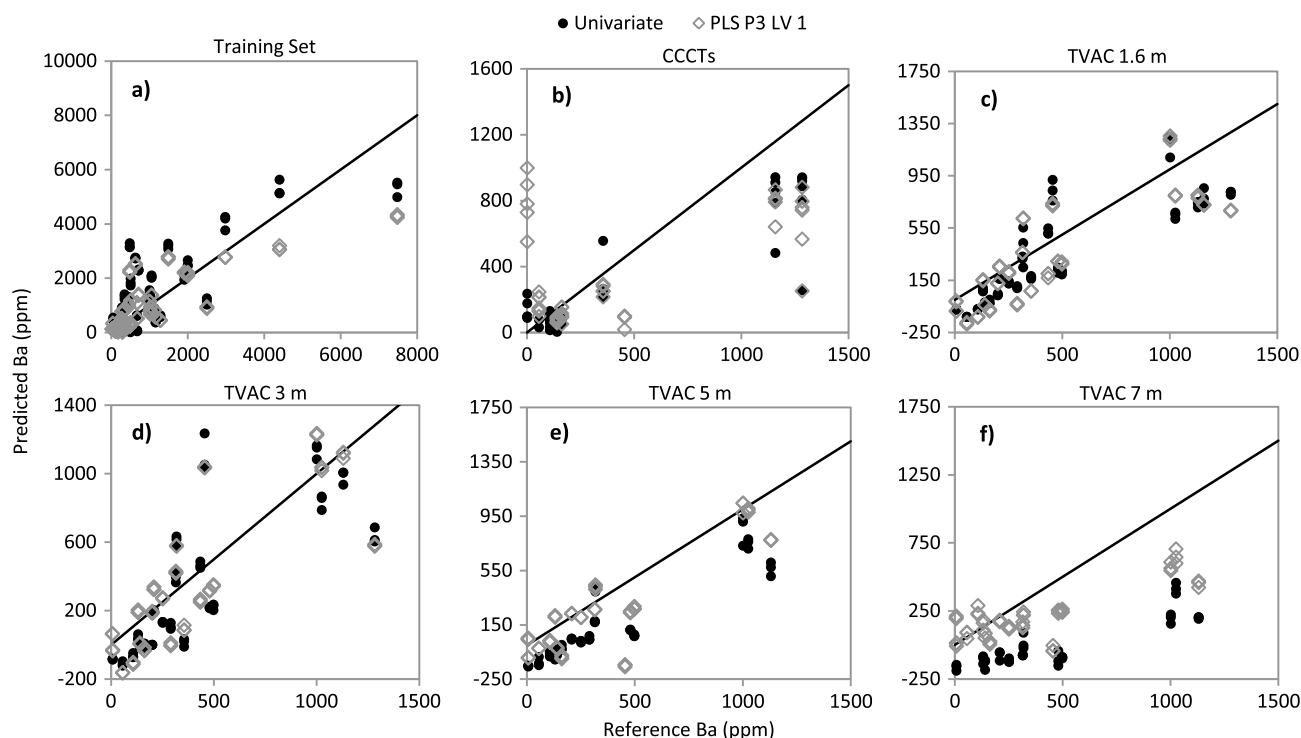
Figure 7. Reference versus predicted composition plots of Ba univariate and PLS models for the (a) RTC training set, (b) the CCCTs, (c) TVAC 1.6 m (d) TVAC 3 m, (e) TVAC 5 m, and (f) TVAC 7 m data sets. Lines indicate 1:1 composition estimates.

versus predicted composition plots (Figure 7) shows the univariate model predicts higher than PLS at concentrations >3000 ppm, while PLS tends to predict higher (and more accurately) at the farther distances in the TVAC set (5 and 7 m). Both the univariate and PLS models poorly predict the Macusanite CCCT but the univariate method is less severe in the overestimation. However, PLS appears to be at least as accurate or more accurate over all of the data sets than univariate modeling. Cases such as Macusanite, in which the PLS is significantly worse than univariate, should be easy to isolate by noting if the peak center is shifted from the Ba position and those abundances can be removed as erroneous. Figure 5b compares the Ba estimates for the PLS P3 model and the univariate model for all Mars samples. The PLS model tends to predict slightly higher values than the univariate and there is considerable scatter between the abundances but there is a fairly good correlation between the two models.

4.3. Strontium

[49] The training set for Sr is fairly complete across a wide concentration range. Standards are available with 30–2800 ppm Sr but the data set is still biased toward the low concentration range with 8 samples above 1000 ppm, 10 samples between 500 and 1000 ppm, and 41 samples below 500 ppm.

[50] There are three viable peaks for use in univariate and reduced wavelength range PLS modeling: Sr II 407.89 nm, Sr II 421.67 nm, and Sr I 460.86 nm (Table 3). Fe lines overlap the 407.89 nm and the 460.86 nm lines; the best line for univariate modeling is at 421.67 nm. The 421.67 nm Sr line is bounded by 2 Fe lines at 421.1 and 422.0 nm; the one to the left does not affect the fit of the Sr line but the one to the right may decrease the quality of the fit for samples

with >~15 wt % Fe_2O_3T. Several samples with high Fe (NAU2-Hi-S, MHC1356, and MHC2319) had poor fits and were not used in univariate modeling. The fitted range for a Voigt profile is from 421.3 to 422.1 nm with a linear background set at the base of the peak. An example of the fit for Picrite and the normalized spectra of the Norite and Picrite CCCTs for the various data sets are shown in Figures 8a and 8b, respectively. There is a slight upward slant to the baseline due to the nearby Fe peak. Sr peaks in the Picrite spectra (1481 ppm Sr) are very similar in size between Mars and the other data sets while the Sr peaks in the Norite spectra (284 ppm Sr) are larger on Mars than in the other data sets. The other CCCTs, all of which have <700 ppm Sr, show similar behavior to Norite, indicating that at lower concentrations, the larger peaks in the Mars data may cause a slight overestimation.

[51] Two univariate models were developed for Sr (Figures 8c–d). Model U1 uses 59 samples of a variety of chemical matrices, with the exception of the three high Fe samples previously mentioned (Table 1). The RMSEP of U1 is 659 ppm (Figure 3c). Examination of the data points that appear to be outliers shows that these points are samples that have chemical compositions that are poorly represented in the database and are dissimilar to the majority of samples, which are igneous or sediments derived from primary igneous minerals. Because of this, the second model (U1-Matrix Matched, or U1-MM) has a reduced suite of samples that includes igneous materials or materials that have an igneous-like suite of major elements. Samples removed from this set include carbonates, sulfates, and Al-clays. This optimizes the model for the type of material typically encountered on Mars. Samples with non-matrix-matched compositions, as determined by the major element compositions, will be predicted on the full
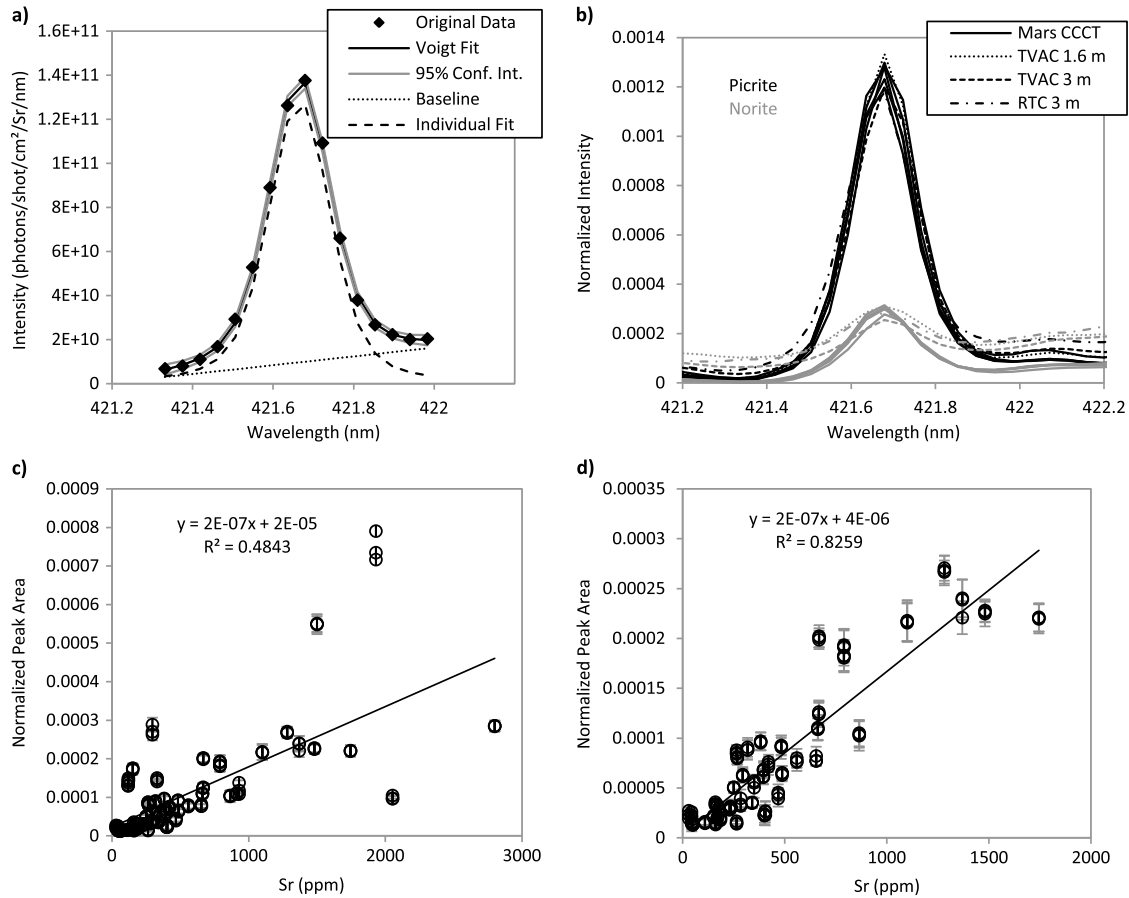
Figure 8. (a) Example Voigt fit of the Sr peak for the training set Picrite spectrum. (b) Comparison of the Mars CCCTs, TVAC 1.6 and 3m, and the RTC training set spectra for Picrite and Norite. (c) Univariate model for all samples and (d) univariate model for igneous and similar matrices.

model, and in the future, matrix-matched models for these rock types may be developed for special cases, such as for carbonates or sulfates. The RMSEP for model U1-MM is 172 ppm. This decrease in RMSEP is due in part to the removal of outliers but it should also be noted that the upper concentration is now 1800 ppm compared to 2800 ppm in U1, and there typically is a decrease in RMSEP as the concentration range is restricted.

[52] A total of four PLS models was built for Sr. Model P1 uses the full wavelength range, and examination of the RMSEP values for the first 20 LVs and the reference versus predicted composition plots for the training and test sets for these LVs indicates the optimal LV is 10. This is one LV more than the global minimum RMSEP for the training set and it minimizes the sum of RMSEPs over all data sets. Estimates for the TVAC data set for LV 10 show the model underestimates at 1.6 m, is fairly accurate at 3 and 5 m, and overestimates above 1000 ppm and underestimates below 1000 ppm at 7 m. The CCCTs are not estimated well with any LV and 10 LVs give negative estimates for abundances below 1000 ppm and positive estimates for abundances above 1000 ppm.

[53] The second PLS model, P2, standardizes and centers the wavelengths. The optimal LV for this model is LV 8, which is one RMSEP before the global minimum RMSEP for the training set and minimizes the overall RMSEP for all sets. For the test sets, LV 8 systematically underestimates the TVAC 1.6 and 3 m sets. For the CCCTs, Macusanite is

overestimated significantly due to what is likely a large Si peak over Sr 407 nm (the SiO_2 content of this sample is 74 wt %) and an unidentified peak that overprints the Sr 460 nm peak. The estimates are fairly accurate for the TVAC 5 and 7 m sets.

[54] The third PLS model (P3) reduces the wavelength range to 27 channels over the three Sr peaks (Table 3) and the optimal LV for this model is 1. The outliers observed in the univariate model are present in the training set predictions and, while additional LVs draw the outliers in (6 LVs are best for the training set alone), the TVAC and CCCT test sets are not well predicted with additional LVs. With one LV, the TVAC 1.6 m set is very well predicted and the TVAC 3 m data are well predicted except for MHC2319, which is overestimated. For the 5 and 7 m TVAC sets, samples with <500 ppm Sr are well estimated but a systematic underestimation, which increases with increasing concentration, begins to occur past 500 ppm. The same overestimation of Macusanite happens with this model as with P2, and the other CCCTs are estimated well up to 1000 ppm. Above 1000 ppm, Picrite shows a small but significant underestimation. Between these three PLS models, both P2 and P3 are very similar but P2 has more scatter in the low abundance range while model P3 appears to be more systematic. Model P3 shot-to-shot abundances on the Mars target Link point 2, which has a large Sr peak, for LV 1 shows that estimates track the Sr 421.7 nm peak intensity.
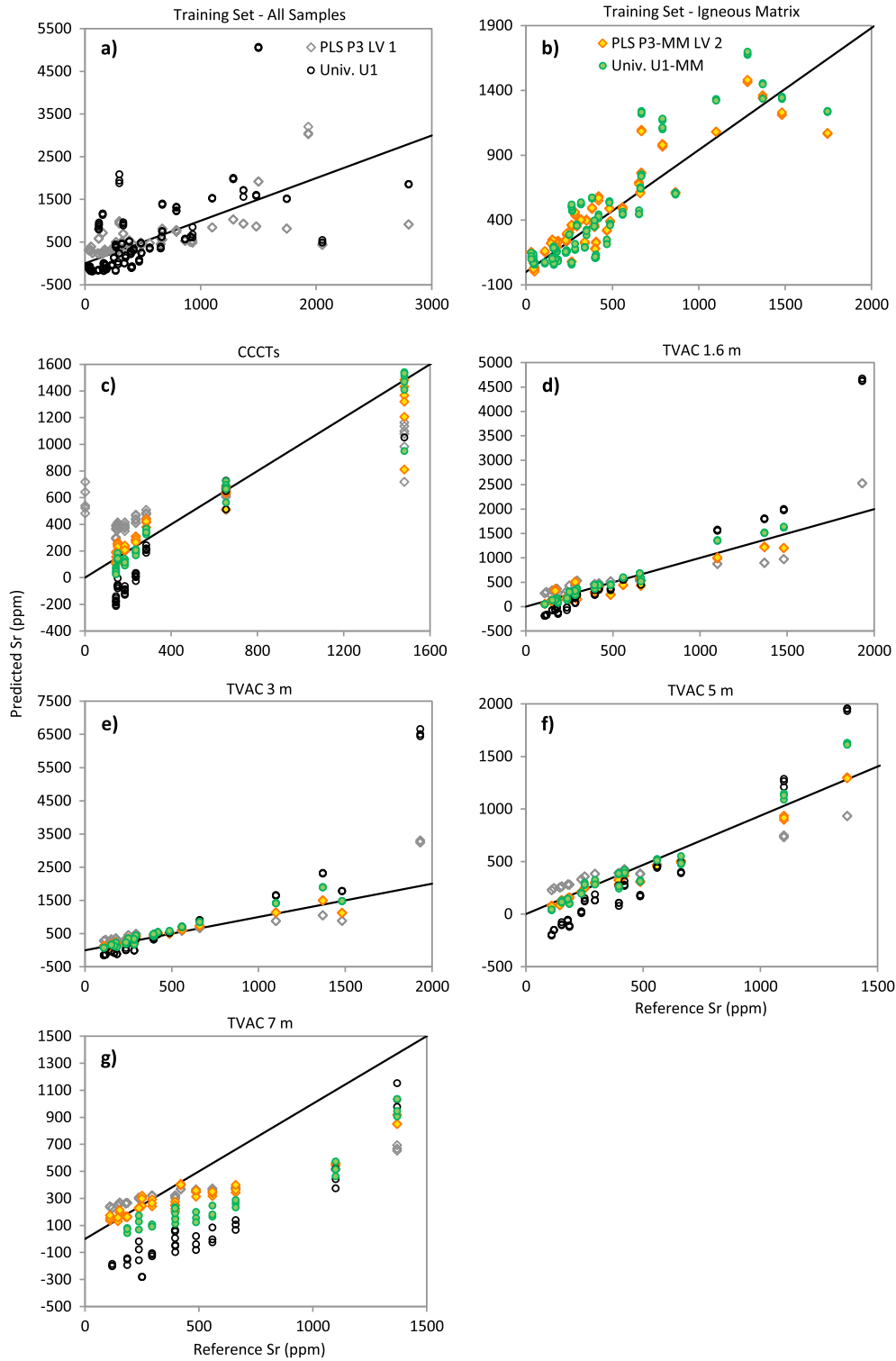
Figure 9. Sr reference versus predicted composition plots for models for (a) the training set and (b) igneous-like matrices. Results for both models for the (c) CCCTs, (d) TVAC 1.6 m, (e) TVAC 3 m, (f) TVAC 5 m, and (g) TVAC 7 m. Lines indicate 1:1 composition estimates.

[55] Finally, Model P3 is rebuilt with the igneous and igneous-like matrix-matched standards in the RTC training set (P3-MM). For the TVAC and CCCT test sets, spectra from samples that appear to be from an atypical matrix based on the major element PLS (i.e., do not contain the typical suite of major elements), namely, the dolomite JDO1, the high Fe and high Si MHC2319 sample, and Macusanite are excluded from the RMSEP calculation. As MHC2319 and Macusanite were outliers in many of the previous models' calculations, this contributes to the change in RMSEP for the two test sets in which it was present (TVAC 1.6 and 3 m for MHC2319 and the CCCTs for Macusanite). Estimates

for the training set appear to be very good up to ~LV 4 where the very lowest concentration range gives increasingly negative results, and this trend increases with the number of LVs. The global minimum RMSEP for the training set is at LV 4 while the lowest RMSEP for the TVAC 3, 5, and 7 m data sets, the CCCTs and the overall sum of RMSEPs are minimized with two LVs. The P3-MM model has fairly stable shot-to-shot estimates for both LV 2 and 4, but two LVs are slightly more consistent than four LVs and therefore two LVs are chosen.

[56] The RMSEPs for the training and test sets (Figure 4c) for the various univariate and PLS models show that the highest error is present in model U1 (all samples), primarily due to the over estimation of MHC2319 in the training set and TVAC 1.6 and 3 m test sets (Figure 9). Removal of this sample for the igneous matrix model (U1-MM), as well as removal of the other sulfates, carbonates, and Al clays, reduces the RMSEP to be on par with the PLS models P2 (standardized) and P3 (reduced wavelength model). Models P2 and P3 are very similar and either would be acceptable for estimating abundances for non-igneous matrices, although it will be preferable to develop specialized training sets for these matrices in the future. Model P3-MM has the lowest RMSEP, primarily due to more accurate estimates in the test sets compared to the U1-MM model. Models P3 (LV 1) and P3-MM (LV 2) will be the primary models to estimate Sr in Mars targets but models U1 and U1-MM will also be used for comparison. Figures 5c and 5d compare the generalized matrix models and igneous-matrix models. For the generalized model (Figure 5c), univariate modeling overestimates relative to PLS at high concentrations and underestimates at low concentrations. For the matrix-matched models, both models are consistent but univariate models estimates are slightly higher across the concentration range.

4.4. Rubidium

[57] The training set has spectra from 53 reference materials with reported Rb concentrations between 0.2 and 2020 ppm (Table 1). GUWGNA (weathered granitic rock) provides the upper limit at 2020 ppm Rb. The next highest sample has a concentration of 860 ppm, followed by 257 ppm, and there are 13 samples between 50 and 300 ppm; the remaining 40 samples are between 0.2 and 50 ppm. Given the small number of samples above 257 ppm, the models presented here focus on the range up to this value, but we recognize that it is possible that this upper bound may be exceeded by observations on Mars. Future additions to the training set will supplement the 50–500 ppm range. Only one CCCT, Macusanite, has sufficient Rb for a visible peak under ChemCam conditions. The Macusanite glass often has poor coupling to the laser and it is very sensitive to the focal distance. At this time, we do not have an independent Rb measurement on the specific piece of Macusanite used for the CCCT but based on the analyses in *Pichavant et al.* [1988], the Rb concentration is expected to be >400 ppm, which is beyond the range of these models.

[58] There are three resolvable Rb emission lines present in spectra taken under ChemCam operating conditions. Rb I 303.3 nm is only present in spectra of GUWGNA and Rb I 794.3 nm is significantly overlapped by an O line, and this latter is excluded from modeling. Rb I 780.2 nm is located near the O I 777 nm unresolved trio of peaks (Table 3). Rb I 780.2 nm is the only viable Rb line for univariate analysis (Figure 10a). Due to the discrepancy in size between O 777

and Rb 780.2, it is difficult to fit a profile to the much smaller Rb line. While fitting both peaks together would be preferable, we found that it was too difficult to consistently fit the Rb line in this manner. Instead, the Rb peak was fit alone by setting a target range of 779.4–781.2 nm (Figure 10b). There were typically 9 or 10 original intensity points in this range and obtaining a consistent fit with so few points was difficult. The PeakFit software has an option to interpolate between points to allow a better, more reliable fit to be achieved, and we used the suggested window point count of five and quadratic fit to interpolate between the original 9–10 points. After interpolation, a total of 30 points was created and the peak and background were fit together to minimize error using a Voigt profile and a linear background at the base of the peak. Of the 53 samples available, only 33 samples had large enough peaks to fit. The Rb I 780.2 nm peak is consistently large enough to be fit down to 21.8 ppm and occasionally fit down to 10 ppm.

[59] The univariate model U1 has an RMSEP of 52 ppm and there are at least two standards that are likely outliers at the high concentration range. JR1 is underestimated, probably due to poor coupling, and VH1 is overestimated for unknown reasons. These samples were left in the model because their removal does not significantly change the estimates due to their balanced distribution relative to the regression line and, while the RMSEP increases, a more conservative RMSEP seems warranted in this case due to the wide spread of data at both the low and high concentration ranges. For the test sets, the Rb I 780.2 peak is well resolved to 5 m but the peak loses form at 7 m (Figure 10a) and the peak is only able to be fit in three samples with the highest Rb shot in the TVAC 7 m set (BK2, SGR1, and JA2) as well as JA3.

[60] Three PLS models were constructed for Rb. Model P1 uses the full wavelength range and examination of the RMSEPs for the first 20 LVs for the training set reveals the global minimum RMSEP occurs at LV 4. This LV also has the lowest RMSEP for the TVAC 1.6, 3, and 5 m sets and the second lowest for the 7 m set and the overall summed RMSEP. However, this model has poor discrimination between high and low concentrations for all but the training set and therefore is an unacceptable model. Model P2 uses the full wavelength range with the wavelength matrix standardized. This model is similar to P1 in that the training set is the only set that has good correlation between predicted and reference compositions. The CCCTs are significantly overestimated for all LVs and the other test sets show no correlation between predicted and reference values. The lowest summed RMSEP is at LV 12, and since this LV has only a slightly higher RMSEP for the training set than the global minimum (35 compared to 29 ppm), LV 12 was selected as the best LV for this model. Lastly, model P3 reduces the wavelength range to 10 channels over two Rb peaks (Table 3). Due to the small number of variables in the X matrix, only 10 LVs are possible. The first six LVs show very good correlation between predicted and reference values with LV 3 having the global minimum RMSEP for the training set. However, LV 2 is very similar in the training set estimates, having an RMSEP of 33 ppm and is also similar in the estimates for the TVAC sets and CCCTs. Both LVs underestimate the mid to high concentration samples for the TVAC 1.6, 5, and 7 m sets and both estimate the 3 m set very accurately. The CCCTs, all with <10 ppm Rb (except
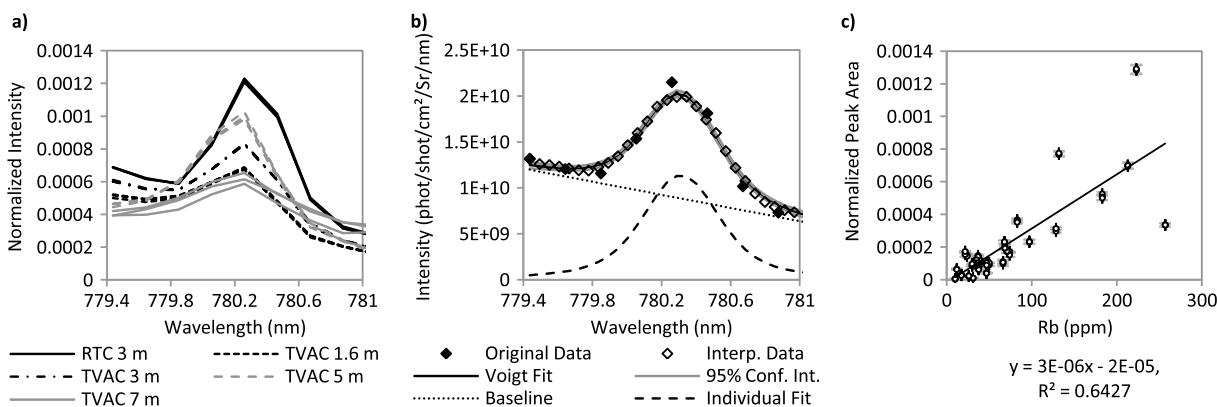
Figure 10. (a) Example spectra of Rb 780.2 nm for the RTC training set and TVAC test sets for SGR-1. (b) Example Voigt fit for the SGR-1 RTC Rb peak; note the upward slant resulting from the nearby oxygen peak. (c) Rb univariate linear model.

Macusanite which is excluded for reasons discussed in the univariate model description), have acceptably low estimates, i.e., < 20 ppm, for both LVs. Overall, of the three PLS models, model P3 is the most accurate (Figure 11). A check of the shot-to-shot estimate consistency on a Mars target using P3 LV 2 and 3 is compared to the Rb 780.26 nm peak intensity for the second point in Link. Both LVs have acceptable shot-to-shot predictions and are consistent with the peak intensity. Because LV 2 has the overall lowest RMSEP for all test sets and only a slightly larger RMSEP for the training set, LV 2 is selected.

[61] Comparing the univariate model to the PLS P3 LV 2 model (Figures 4d and 11), it appears the PLS model is more accurate than the univariate model. The error on the univariate model is higher than model P3 for all test sets but is particularly high for the TVAC 5 m set. The high error is primarily due to BK2 and these fits were checked and appear to be accurate. Comparison of the two models for all Mars analysis locations (Figure 5d) shows that the univariate model overestimates relative to the P3 model at abundances >100 ppm and underestimates slightly at abundances <50 ppm. Both methods will be applied to the Mars targets for quality control. One of the benefits of using PLS is that compositions may be estimated for targets that do not have a peak large enough to fit a profile. A detriment to PLS is that the background around the primary Rb peak fluctuates with the O 777 nm peak intensity and this may result in Rb estimates that are more related to the fluctuation in the
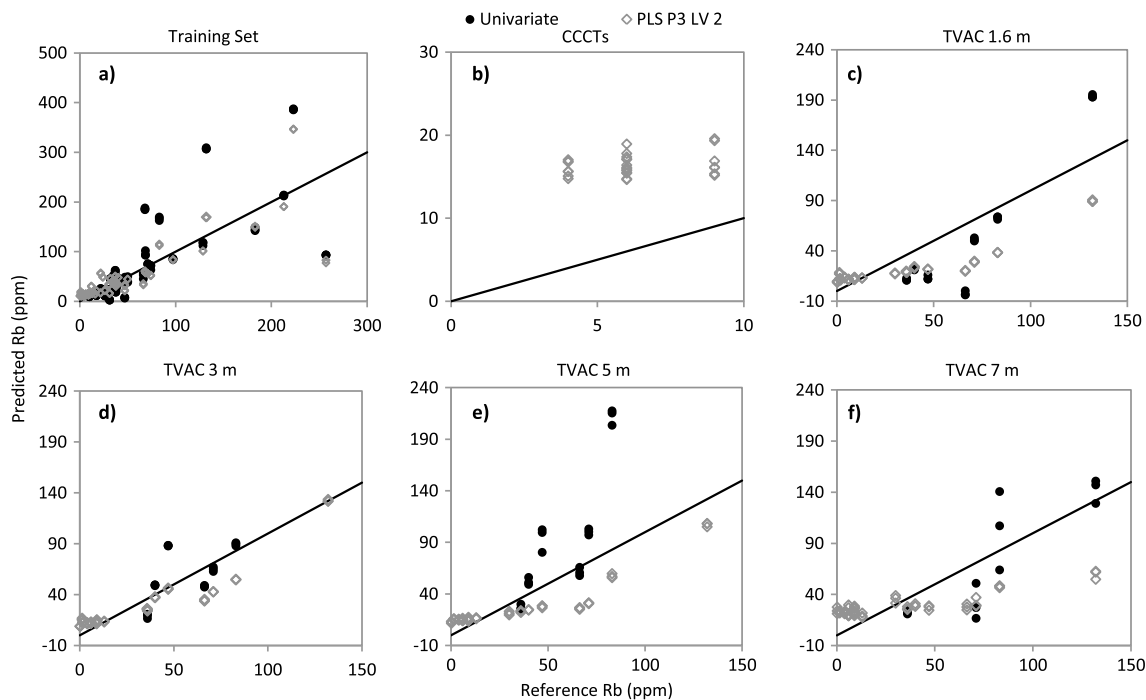

Figure 11. Reference versus predicted composition plots for Rb comparing the univariate model to the PLS P3 LV 2 model for the (a) RTC training set, (b) CCCTs, (c) TVAC 1.6 m, (d) TVAC 3 m, (e) TVAC 5 m, and (f) TVAC 7 m. Lines indicate 1:1 composition estimates.

Table 4. Trace Element Summary for Bradbury and Rocknest Targets[a]

	n	Mean (1σ)		Median		Range	
		Univariate	PLS Model	Univariate	PLS Model	Univariate	PLS Model
Li (RMSEP: 40 ppm Univariate and PLS)							
Link (Conglomerate)	5	<5 (0)	<5 (0)	<5	<5	<5–10	<5
Pebble	15	10 (10)	<5 (10)	10	<5	<5–30	<5–30
Rock, Bradbury	42	10 (10)	<5 (10)	10	<5	<5–40	<5–50
Rock, Rocknest	128	10 (10)	10 (10)	10	<5	<5–60	<5–80
Sand	63	<5 (0)	<5 (0)	<5	<5	<5–10	<5
Soil	35	10 (10)	<5 (10)	10	<5	<5–30	<5–30
Sr (RMSEP: 170 ppm Univariate, 160 ppm PLS)							
Link (Conglomerate)	5	1680 (400)	1270 (320)	1800	1380	1180–2190	860–1670
Pebble	15	320 (140)	220 (110)	300	210	80–560	bd–370
Rock, Bradbury	36	180 (130)	90 (110)	150	40	bd–480	bd–340
Rock, Rocknest	99	90 (70)	50 (50)	80	50	bd–310	bd–230
Sand	63	100 (60)	10 (20)	80	bd	20–290	bd–130
Soil	35	100 (50)	40 (60)	90	bd	10–300	bd–200
Ba (RMSEP: 640 ppm Univariate, 670 ppm PLS)							
Link (Conglomerate)	5	190 (120)	270 (40)	140	260	70–330	220–320
Pebble	15	50 (90)	110 (160)	bd	40	bd–280	bd–560
Rock, Bradbury	42	70 (130)	140 (210)	10	60	bd–610	bd–1010
Rock, Rocknest	121	10 (20)	10 (30)	bd	bd	bd–150	bd–170
Sand	63	20 (90)	60 (90)	bd	30	bd–670	bd–570
Soil	34	20 (30)	50 (60)	bd	20	bd–80	bd–210
Rb (RMSEP: 50 ppm Univariate, 30 ppm PLS)							
Link (Conglomerate)	5	210 (50)	160 (30)	210	170	160–270	130–190
Pebble	12	30 (50)	40 (40)	10	30	bd–150	20–120
Rock, Bradbury	34	20 (20)	30 (10)	10	30	bd–80	20–70
Rock, Rocknest	64	10 (10)	20 (10)	bd	20	bd–30	20–40
Sand	17	10 (20)	20 (10)	bd	20	bd–70	20–60
Soil	13	10 (20)	30 (10)	bd	20	bd–70	20–60

[a]Abundances and RMSEP values have been rounded to the nearest 10 ppm. bd = below detection.

size of the O peak than to Rb. This will be discussed further in the Rb section of Mars results.

5. Mars Results and Discussion

5.1. Overview of the Mars Data Set

[62] Over the first 100 sols, ChemCam analyzed ~50 rock and soil targets. For this study, data collected prior to sol 49 are considered to be part of the Bradbury region while data taken after sol 49 are part of the Rocknest region. Each ChemCam analysis point typically has a mini-depth profile of 30 shots although occasionally up to 600 shots were taken at each point to search for coatings or layering; <1 μm is removed per shot and is dependent on material type [*Wiens et al.*, 2012]. In this study, we use abundances based on averaged spectra for each point, excluding the first five shots to remove all or most of the dust as well as abundances from single-shot data. Initially, ChemCam began with single point observations for the rocks Coronation, Stark, and Mara. After confirming the successful operation of the instrument, larger line scans and then raster grids were developed from 1 × 5 up to 5 × 5 points, although 3 × 3 is the most common configuration. Spectra collected from targets at > ~4.5 m are noisier than those represented in the training set (which was taken at 3 m) and, until distance effects have been studied further, these spectra have been removed from the current study. Also, in some cases, the laser struck a hole or missed focusing on the intended target resulting in poor signal to noise ratios and these spectra were removed from the data set as well. For this study, we have divided the Mars targets into five general categories: rocks, pebbles, Link (conglomerate), sand (which includes both the Akaitcho

aeolian sand ripple and the Rocknest sand shadow), and soils. It can be difficult to determine if the analysis location struck a pebble or soil [*Meslin et al.*, 2013], and the best attempts were made to properly distinguish them using post-LIBS RMI imagery or the shot to shot spectrum behavior. The Rocknest sand shadow was analyzed by multiple instruments, including SAM [*Leshin et al.*, 2013], CheMin [*Bish et al.*, 2013; *Blake et al.*, 2013] and APXS [*Schmidt et al.*, 2013].

[63] A total of 288 analysis points is used in this study. As a guideline, we do not assume that an element is present based only on predicted values from a PLS model since those estimates are highly dependent on the training set. All major elements as well as Li have peaks visible in every location but Rb, Sr and Ba do not. Eight spectra have no obvious Ba; this number is likely low due to the uncertainty in identifying what peaks are present in its characteristic spectral regions. Thirty-five spectra have no Sr peak or the peak is too small to be fit. Due to the nearby oxygen peak and the relatively low level of Rb in most rocks and soils, 143 spectra do not have large enough Rb peaks to fit. A summary of the trace element data is shown in Table 4. Major and trace element results for specific targets discussed in the text are presented in Table 5. Note that the trace element abundances in the following text and these two tables have been rounded to the nearest 10 ppm; averages and standard deviations in Table 4 were calculated prior to rounding.

[64] In the following sections, we discuss notable occurrences of Li, Ba, Rb, and Sr. Because the highest abundances of Rb and Sr occur together, those sections are combined. The conglomerate, Link, will be discussed in this section due to its unique Rb and Sr abundances. Because of the error

Table 5. Major and Trace Element Abundances for Selected Gale Crater Targets[a]

	SiO_2	TiO_2	Al_2O_3	FeOT	MgO	CaO	Na_2O	K_2O	Sr (Univ.)	Sr (PLS)	Li (Univ.)	Li (PLS)	Rb (Univ.)	Rb (PLS)	Ba (Univ.)	Ba (PLS)
RMSEP	7.3	0.6	3.9	3.2	4.6	4.2	0.7	1.0	170	160	40	40	50	30	640	670
						High Li Observations										
JakeM 1	53.4	-	10.7	15.5	6.5	-	4.6	1.0	-	-	**40**	**50**	10	20	-	-
Rocknest3a 8	44.1	1.2	10.3	21.9	2.0	0.3	3.0	1.0	70	110	**60**	**80**	-	20	-	-
Rocknest_3_Top1 2	40.6	0.5	7.6	17.1	2.8	3.9	3.0	0.5	20	-	**40**	**40**	-	20	-	-
Bathurst 1	39.1	1.1	7.6	16.3	11.6	5.3	2.3	0.3	120	10	**50**	**60**	10	30	-	-
Bathurst 2	39.9	1.1	6.8	15.5	8.8	6.5	2.0	0.9	210	60	**40**	**50**	30	40	20	-
Bathurst 3	41.9	1.0	7.4	14.7	10.5	5.5	2.4	0.9	300	110	**30**	**40**	20	30	110	140
Bathurst 4	42.1	1.2	7.3	16.3	10.1	4.5	2.4	1.1	200	50	**40**	**60**	20	40	20	10
Bathurst 5	39.8	1.3	7.6	16.8	10.7	5.5	2.2	0.6	170	50	**30**	**40**	20	30	-	-
						Variable Ba Observations										
Stark	72.4	0.9	7.6	7.9	-	3.6	2.8	2.3	120	-	-	-	60	50	**550**	**740**
Thor_Lake 5	36.1	3.3	12.5	23.1	4.1	-	1.8	0.7	-	-	-	-	-	20	-	140
JakeM_1 4	43.9	0.4	7.5	15.0	2.1	9.1	2.9	0.7	-	-	-	10	10	20	-	-
Akaitcho 7	51.1	0.7	10.4	11.6	4.2	5.1	3.1	1.5	250	50	-	-	20	30	**670**	**570**
Preble 1	63.2	0.5	6.8	11.2	-	5.7	2.8	1.8	170	-	-	-	30	40	180	530
Preble 3	62.6	0.4	9.3	12.3	-	3.2	3.0	1.8	170	20	-	-	20	30	230	390
						High Rb and Sr Observations										
Link 1	65.4	0.7	14.6	9.0	-	5.8	2.6	2.1	**1800**	**1380**	10	-	**270**	**170**	100	220
Link 2	66.3	0.7	13.3	8.0	-	6.9	3.0	1.9	**1380**	**1020**	10	-	**210**	**170**	70	270
Link 3	64.7	0.6	16.3	9.2	-	4.3	2.4	2.2	**2190**	**1670**	-	-	**250**	**190**	330	260
Link 4	67.3	0.6	13.5	4.7	-	7.9	3.6	2.4	**1180**	**860**	-	-	**160**	**130**	140	250
Link 5	62.2	0.4	14.0	11.9	-	3.6	2.3	1.9	**1860**	**1400**	-	-	**160**	**130**	300	320
Beaulieu 2	69.5	0.7	10.2	7.6	-	4.4	4.2	2.6	**520**	**340**	10	-	**150**	**120**	90	160
Beaulieu 3	70.8	0.8	10.8	6.8	-	6.5	3.3	1.7	**510**	**210**	10	-	**120**	**110**	280	370
Taltheilei 4	65.3	0.6	9.9	8.5	-	6.5	3.7	2.0	**440**	**170**	10	-	**60**	**70**	190	460
						High Rb Observations										
Preble 2	79.7	0.3	13.9	5.5	-	-	3.8	3.6	-	100	10	-	**80**	**70**	610	1010
JakeM_1 5	67.9	-	11.9	11.2	-	0.8	4.7	2.5	220	80	10	-	**60**	**60**	70	70
Anton 2	48.2	0.7	9.7	10.9	9.3	7.2	3.3	0.5	130	30	10	-	**70**	**60**	-	100
Akaitcho 2	45.1	0.5	10.1	12.4	5.9	6.4	2.7	0.6	90	-	-	-	**70**	**60**	60	40
						High Sr Observations										
Murky 2	68.5	0.4	11.9	5.7	-	10.9	4.2	1.6	**440**	**330**	10	-	-	20	-	40
Taltheilei 1	63.4	0.3	11.2	9.4	-	7.5	3.9	1.3	**440**	**180**	10	-	-	20	160	280
Taltheilei 5	63.4	0.3	10.9	7.9	-	10.1	3.6	1.3	**480**	**230**	10	-	-	20	100	250
Kam 5	67.4	0.6	10.2	6.5	-	11.0	3.8	1.6	**560**	**370**	-	-	30	40	-	70
JakeM 3	65.7	0.1	12.5	14.1	-	1.4	4.2	2.0	**410**	**290**	-	-	10	20	120	60

[a]Major element abundances are from the PLS2 analysis described in *Wiens et al.* [2013]. Some targets may fit in multiple categories. Notable instances of trace elements in bold. Observation number is listed after the target name. Trace element abundances and RMSEP values have been rounded to the nearest 10 ppm. Dashed lines indicate abundances are too low to be estimated with the current models.

and uncertainty in Ba, at this time we only present high level results until the region with the primary Ba peak is more accurately represented in the training set.

5.2. Lithium

[65] Overall, Li is low for the majority of rocks and soils at Bradbury and Rocknest (Table 4). For the following results, the univariate model with an RMSEP of 40 ppm is used unless otherwise specified. As previously discussed, the univariate model predicts the low values better than the PLS model due to fewer negative concentrations but may underestimate the higher values. Here we choose to focus on three observations: (1) the Li abundance in soils and sand is low, ~5 ppm; (2) Li abundances in several discrete locations in two rocks, Jake_M and Rocknest_3, have Li concentrations that are detected >30 ppm; and (3) Bathurst_Inlet has >30 ppm Li at all five locations analyzed and, in locations 3–5, Li decreases in abundance over the 30 shot depth profile, indicating it is enriched at the surface.

5.2.1. Lithium in Soils

[66] Since Viking first analyzed soils at two locations on Mars and found enrichments in S and Cl at both locations

[*Toulmin et al.*, 1977], there has been considerable work to determine the origin of the soils. Soils at both locations, as well as soils analyzed by later missions including the MERs, are similar in composition, an observation that has been interpreted to be the result of global homogenization by aeolian processes [*Toulmin et al.*, 1977; *Ming et al.*, 2006; *Morris et al.*, 2006a, 2006b, 2008; *Yen et al.*, 2005, 2013]. Chemical analyses of the fine soils by Viking indicate the presence of a two component system: a silicate/Fe-oxide component of basaltic origin and a component enriched in S and Cl, which was interpreted to be a salt [*Clark and Baird*, 1979; *Clark and Van Hart*, 1981]. Recent results from CheMin on the <150 μm fraction of the Rocknest sand shadow support this two component system and reveal a predominantly basaltic mineralogy with a crystalline component consisting of plagioclase, forsteritic olivine, augite and pigeonite, plus an amorphous component that comprises ~25-30 wt % of the XRD analysis [*Bish et al.*, 2013]. The presence of mafic igneous materials was anticipated due to the near absence of evidence for evolved magmas on Mars [cf. *Bandfield et al.*, 2004], whereas the S- and Cl-bearing phase has been more puzzling. *Morris et al.* [2013] indicate that the
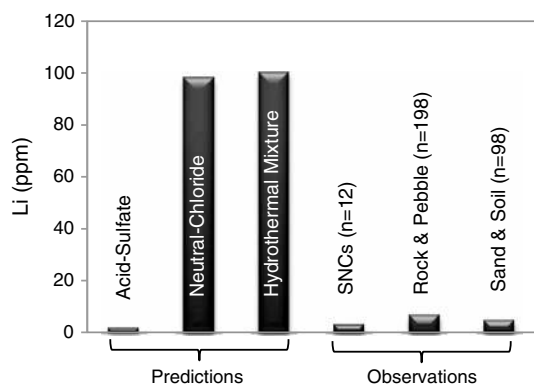
Figure 12. Li soil predictions in Martian soil from *Newsom et al.* [1999] compared to averaged SNC, Rocknest, and Bradbury rocks, pebbles, soil, and sand data. The upper range for the Gale rocks and pebbles is ~60 ppm and for sand and soils is ~30 ppm (RMSEP = 40 ppm, Table 4). Measured values in the Gale crater soils indicate that the predicted enrichment in Li from the neutral chloride and hydrothermal mixture models is not present, and are consistent with the acid sulfate soil formation model, where S can be transported to the surface by vapor phase transport, but not Li.

amorphous phase(s) observed by CheMin, rather than crystal-line sulfides, sulfates, and chlorides, likely host most of the S and Cl. It is unclear what this S- and Cl-bearing phase is, but if it is a noncrystalline salt or superficial coating on grains, the previously hypothesized mechanisms of formation may be evaluated based on associated Li observations. Deposition of volatile constituents via volcanic aerosols has been posited as a likely mechanism for the formation of the S- and Cl-bearing component because this mechanism requires little or no water [*Clark and Baird*, 1979; *Banin et al.*, 1997]. Alternatively, the components may have been acquired via hydrothermal fluids, enriching the surface materials in fluid mobile elements such as Li [*Newsom et al.*, 1999].

[67] *Newsom et al.* [1999] modeled two common forms of terrestrial hydrothermal systems, the acid sulfate and neutral chloride systems. In the former, water is limited and deeply buried water is vaporized by heat from a magma source. This vapor rises, mobilizing elements such as S and Cl to the surface. In the neutral chloride system, water enriched in fluid-mobile elements forms springs on the surface and newly formed precipitates are enriched in mobile elements, such as Li and Cl. *Newsom et al.* [1999] found that a combination of these two systems could match the S/Cl ratio observed by Viking. They note that the volcanic aerosol formation mechanism has highly variable S/Cl ratios and additional information is required to determine the viability of this mechanism. Several chemical signatures for fluid-mobile and vapor-mobile formations were identified in *Newsom and Hagerty* [1997]. If hydrothermal fluids reaching the surface are primarily responsible for the salt component, Li is expected to be enriched up to ~100 ppm in the soils [*Newsom et al.*, 1999]. Figure 12 shows the Li abundance predictions for the acid sulfate hydrothermal system, neutral chloride system, and a mixed system compared to observations in the average whole rock SNC meteorites (~3.3 ppm, based on 12 analyses in *McSween* [2003], *Filiberto et al.* [2012 and references therein], *Chennaoui Aoudjehane et al.* [2012], and *Barrat et al.* [2002])

and the Gale crater materials. Li values are low in the meteorites and Gale materials, inconsistent with the predicted values for models involving fluids reaching the surface. The Li values are more consistent with a vapor-transport mechanism, either via the acid-sulfate hydrothermal system or volcanic aerosols.

[68] Results are inconclusive as to which vapor-transport mechanism is more likely. *Newsom and Hagerty* [1997] proposed volcanic aerosol deposition may show increased Zn, Mo, Cd, Ba, and W relative to hydrothermal acid sulfate deposition. ChemCam's detection limit for these elements is high, and other than Ba, none have been positively detected in Gale crater. APXS has detected up to ~2250 ppm Zn in rocks at the MER Gusev site and up to ~1100 ppm in rocks at Gale crater site [*Schmidt et al.*, 2013 and references therein]. Soils at both locations have around ~350 ppm Zn [*Schmidt et al.*, 2013 and references therein]; these are relatively high abundances that may be evidence for volcanic aerosol deposition. Volcanic aerosols may be the primary contributor to the salt component because such systems have variable S/Cl while acid sulfate hydrothermal systems have a more consistent ratio that does not match with the Viking observations.

5.2.2. Lithium in Rocks

[69] The averaged Li abundance and standard deviation for all rocks and pebbles in the Bradbury and Rocknest traverse is 10 ppm ± 10 (1σ, Table 4). This is lower than the terrestrial upper continental crust, which is estimated to have ~24 ppm ± 7.6 (1σ) Li [*Rudnick and Gao*, 2003]. Li is higher in the terrestrial crust which is andesitic overall, unlike Mars which is basaltic. Also, Li is a fluid mobile lithophile element that may be redistributed on Earth due to abundant water, unlike present-day Mars. The observed Li abundances at Gale are consistent with estimates for the Earth's mantle (~1.5 ppm [*McDonough and Sun*, 1995; *Magna et al.*, 2006]), mid-ocean ridge basalts (MORB, ~4–5 ppm [*Tomascak et al.*, 2008; *Chan et al.*, 1992]), and with the average whole rock SNC value (~3.3 ppm).

[70] There are three observation points in the first 100 sols (excluding Bathurst Inlet, which is discussed in the following section) that have Li abundances >30 ppm, found in Jake_M (inferred igneous float) and Rocknest_3 (vesicular rock); Li peaks from these points compared to other spectra of low Li abundance (Coronation rock and Portage soil <10 ppm) are shown in Figure 13a. Point one in the sol 45 1 × 5 of Jake_M has an estimated Li abundance of 40 ppm (univariate) and 50 ppm (PLS). Point eight in the sol 83 1 × 10 (Rocknest_3a) of Rocknest_3 has between 60 (univariate) and 80 ppm (PLS) while point two on the top of the same rock in the sol 88 5 × 5 analysis (Rocknest_3_Top1) has 35 (univariate) to 40 ppm Li (PLS). These points have midrange SiO_2 (40–54 wt %), Al_2O_3 (7–11 wt %), and MgO (3–7 wt %). FeOT and Na_2O are relatively high (>16 wt % and 3–4 wt %, respectively) and CaO is somewhat low (<4 wt %). The RMSEP for both Li models is 40 ppm and major element RMSEPs are given in Table 5.

[71] Attempts to constrain mineralogical possibilities as a host for Li through element correlations were made through inspection of single-shot intensities for major and trace element species compared to Li peak intensity. This method is most successfully applied when changes occur with depth. The point in Jake_M and the sol 88 point two analysis on Rocknest_3_Top1 do not show significant changes over the
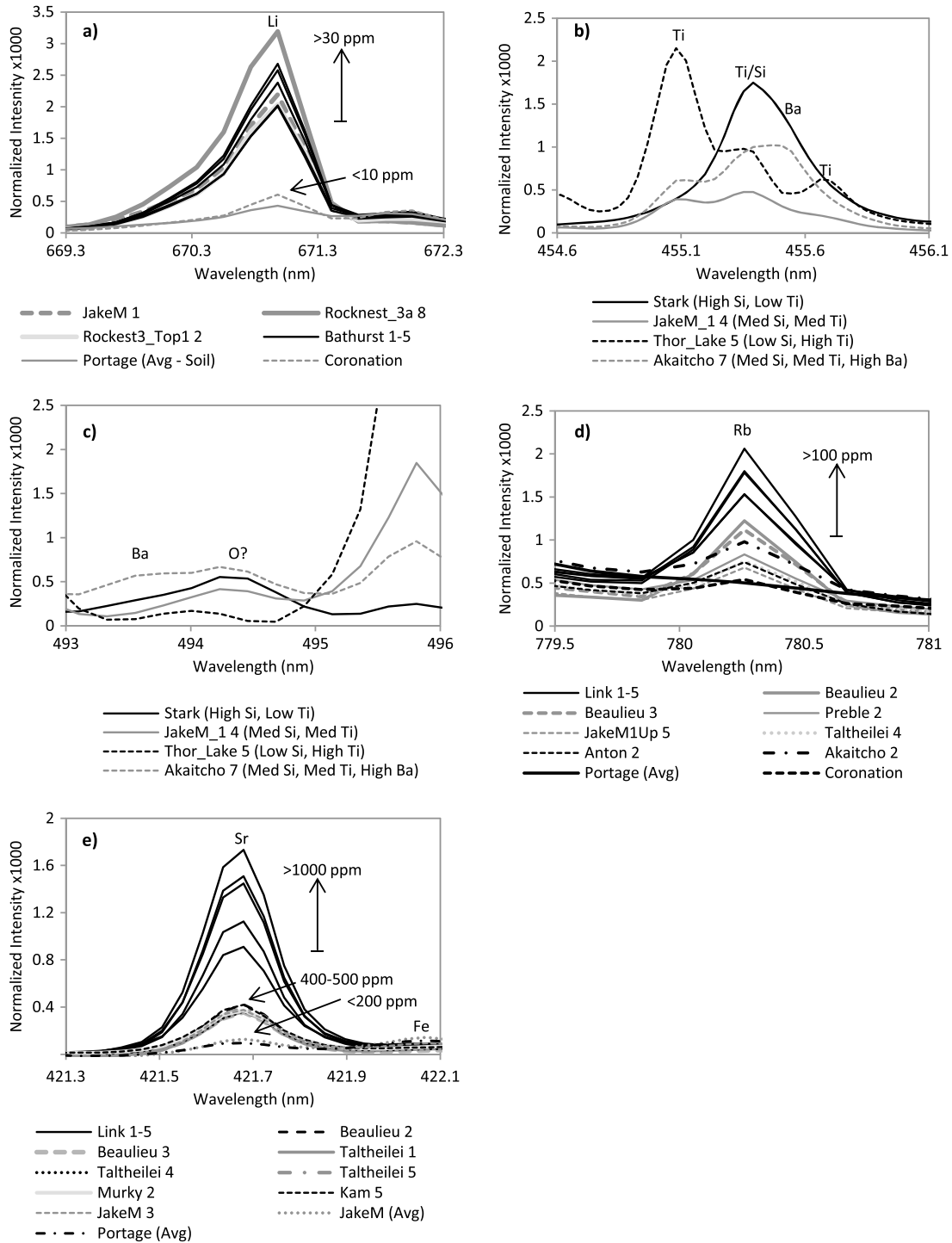
Figure 13. Example spectra for notable observations of (a) Li with Portage soil and Coronation (both <10 ppm Li) for comparison, (b) Ba 455.5 nm, (c) Ba 493.5 nm, (d) Rb with Portage soil (<20 ppm) and Coronation (~30 ppm) for comparison, and (e) Sr with the averages of Portage soil and JakeM for comparison (both <200 ppm).

30 shot profile and therefore it is difficult to determine what elements correlate with Li. Point eight in Rocknest_3a does show a small compositional change over 30 shots and therefore the subsequent discussion will focus on this point alone. Element correlation analyses can be done using PLS estimates or using peak intensities. In instances where certain major elements have low abundances, it is often more useful to select specific emission lines for correlation analysis instead of using absolute abundances due to the uncertainty in estimates at low abundances. The selected lines have been checked to ensure they have a linear relationship with abundance using the training set and these lines are often less intense emission lines, which suffer less from nonlinearities. When available, several lines are used to verify results. In the
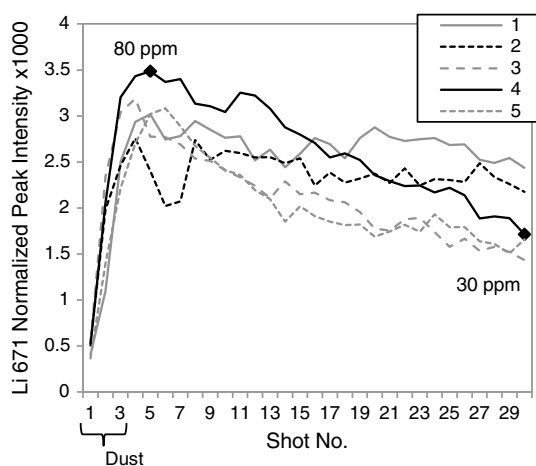
Figure 14. Li 671 nm peak intensity trends with depth in the five analysis points taken on Bathurst_Inlet. PLS estimates for the maximum and minimum peak height for point 4, which shows the largest decrease, are 80 and 30 ppm (RMSEP 40 ppm), respectively.

case of Rocknest_3a point eight, Mg and Ca abundances are relatively low and therefore peak intensities are used instead of PLS estimates.

[72] Analysis of element correlations with Li over the small depth profile at Rocknest_3 point eight reveals that Si, Al, Sr and Mn correlate positively with Li while Ti, Cr, and Mg correlate inversely. Most of these correlations are not strong, with an R^2 on the order of 0.32 to 0.40 for Si, Al, and Sr. Inverse correlations with Ti, Cr, Mg, and Mn have a slightly higher R^2 (0.46 and 0.63). Fe, Na, and K show little correlation with Li. The strongest correlation ($R^2 = 0.63$) is an anticorrelation between Li and Mg.

[73] If these correlations are not spurious, they suggest Li may be associated with an aluminosilicate, possibly a clay mineral, which may be indicative of aqueous alteration, or it may be in a primary igneous mineral such as pyroxene. Li may be enriched in smectite clays, i.e., montmorillonite and hectorite, where Li may substitute for Mg or it may be adsorbed in the interlayer region [*Horstman*, 1957; *Vigier et al.*, 2008]. Alternatively, Li may be hosted in an Mg-pyroxene. In this situation, Li would be incorporated into the mineral structure at time of formation and the small compositional change with depth may indicate that the depth profile partially traversed a zoned grain or it is simply an artifact of the ablation process sampling slightly different material with each laser pulse. Pyroxenes may incorporate significant Li into their structure but no Li-enriched grains have been identified in the SNC meteorites [e.g., *Beck et al.*, 2004, 2006; *Barrat et al.*, 2002; *Herd et al.*, 2005; *Lentz et al.*, 2001].

[74] Examination of Rocknest_3's morphology and texture does not conclusively indicate if it is sedimentary or igneous in origin; layers or striations are present but such features could be solidified lava flow features or sedimentary layering [*Schmidt et al.*, 2013]. If Rocknest_3 is an igneous rock, the element correlations in point 8 may indicate that a mineral grain that was fully or mostly sampled has been partially altered from a primary igneous mineral and the alteration product is enriched in Li. It is also possible that the grain is unaltered primary material that is enriched in Li. If

Rocknest_3 is a sedimentary rock, the grain may be detrital in origin due to its uniqueness among the nearly 40 analysis points obtained on this rock. In this case, the grain may be unaltered igneous material or a grain weathered to an aluminosilicate clay. Additionally, point eight in Rocknest_3 is the first point to sample the putative layers in the upper part of Rocknest_3 [*Tokar et al.*, 2013]. It is possible that this may be a layer formed of material enriched in Li while the other sampled layers consist of material lower in Li content.

5.2.3. Lithium in Bathurst_Inlet

[75] Bathurst_Inlet was analyzed with a 1 × 5 ChemCam linescan and in two locations by APXS. Images taken by the Mars Hand Lens Imager (MAHLI) reveal that the Bathurst Inlet bedrock unit is fine grained (<80 μm) [*Schmidt et al.*, 2013]. The five locations analyzed by ChemCam show Bathurst Inlet to be chemically homogeneous over the LIBS beam size compared to Jake_M and the Bradbury float rocks discussed by *Sautter et al.* [2013]. Bulk composition of SiO_2 and alkalis from APXS indicates Bathurst Inlet is a hawaiite and ChemCam data are consistent with this [*Schmidt et al.*, 2013]. One distinctive feature is its relatively high K abundance, such that K/Na > 1 [*Schmidt et al.*, 2013]. Another unique feature of Bathurst_Inlet is its relatively high Li (>30 ppm) at each of the five analysis points. Spectra of its Li peaks compared to other Mars targets are shown in Figure 13a.

[76] ChemCam points 3–5 show a pronounced decrease in Li abundance with depth (Figure 14), from ~80 ppm after the dust has been removed to 30 ppm (PLS, RMSEP = 40 ppm) at shot 30 in point four. Other elements do not show such a marked change with depth. In each location, Si, K, Na, and Rb appear to correlate positively with Li (Figures 15a and 15b), with the strongest correlations in point four (R^2 0.51-0.87). There is a weaker inverse correlation between Li and Mg (R^2 0.38–0.48). Calculation of the percent change between averaged PLS results for major and trace element PLS abundances over shots 6–10 compared to shots 26–30 shows that Li, Rb, K, and Na have the largest change with depth (Figures 15c and 15d).

[77] Two potential scenarios may explain these results. Because the alkali abundances correlate, a possible interpretation is that the depth profiles are sampling areas with increasing abundance of alkali-rich feldspar, feldspathoids, or mica grains. Alternatively, the favored scenario is that the Bathurst unit has undergone alteration via a process that has mobilized the highly soluble alkalis toward the surface, as observed in the ~15 μm depth profile. Many factors influence element mobility including composition, mineralogy, pH, temperature, etc., making it difficult to parse out relative mobility among elements when these factors are unknown. However, the alkalis (Li, Rb, Na, and K) are generally considered to be more fluid mobile than elements such as Al and Ti [e.g., *Nesbitt and Wilson*, 1992]. The observed pattern of increasing alkalis toward the surface is consistent with this. Li is the most fluid mobile element and also demonstrates the largest change with depth. This enrichment process may proceed via periodic wetting over a long period of time, possibly from frost, and subsequent evaporation/sublimation would carry Li and the other alkalis upward. Surficial alkali and alkali earth enrichments (e.g., Rb, Na, K, and Ca) have been observed in weathered Antarctic meteorites by *Velbel et al.* [1991]. Their preferred explanation is that the meteorites have
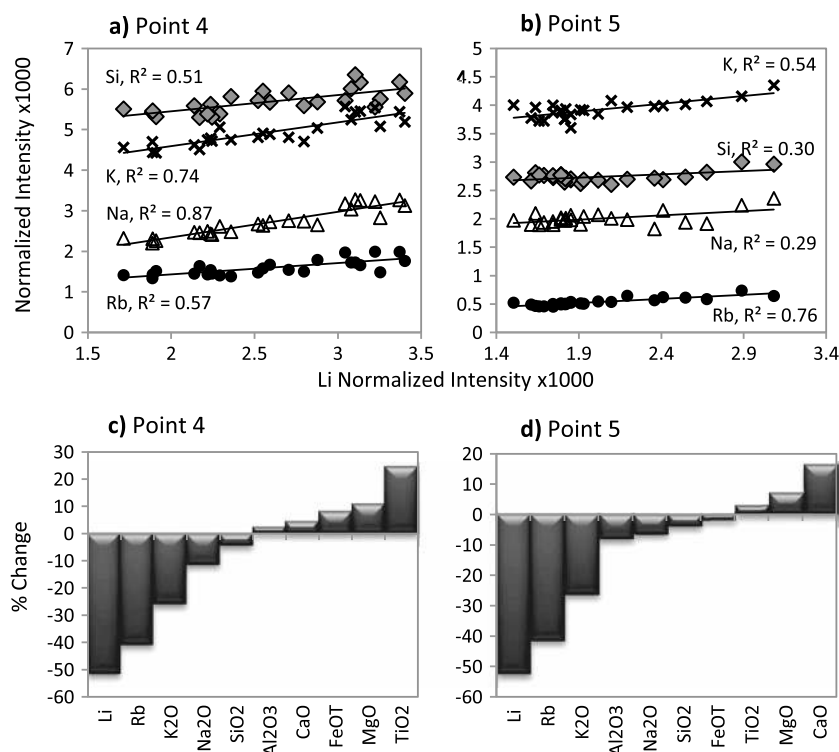
Figure 15. Single-shot normalized peak intensity data for Bathurst_Inlet analysis points (a) four and (b) five and percent change with depth calculated from the average of shots 6–10 and shots 26–30 using PLS major and trace abundances for points (c) four and (d) five. Si, Na, K, and Rb correlate positively with Li peak intensity. Some peaks have been scaled; plotted are Si 635 nm, Rb 780 nm, K 767 (÷3) and Na 819 nm. Note that intensities are not representative of absolute abundance. For major elements, smaller peaks are chosen because they are less susceptible to saturation and self-absorption. From the percent change plots, the largest decreases with depth are in Li, Rb, and K_2O.

undergone leaching and evaporation that led to the formation of evaporites on the exterior of the meteorites. A surface enrichment in Ca is not observed in Bathurst_Inlet and no Li data are provided in *Velbel et al.* [1991] but the situations may be analogous.

5.3. Barium

[78] Float rocks and pebbles sampled early in the traverse at the Bradbury site are, on average, somewhat enriched in Ba relative to rocks sampled at the Rocknest site (Table 4), consistent with the more felsic nature of the Bradbury rocks [*Sautter et al.*, 2013]. For example, the average Ba abundance and standard deviation for the group's average for the 36 analysis points on rocks at the Bradbury location is 70 ± 130 ppm (1σ, univariate) or 140 ± 215 ppm (1σ, PLS) compared to 5 ± 20 ppm (1σ, univariate) or 10 ± 30 ppm (1σ, PLS) over the 121 points on Rocknest rocks. However, because the detection and quantification of Ba is difficult, in this section we focus only on the clearest detections of Ba. A clear detection is defined by the obvious presence of peaks at both the primary Ba location at 455.5 nm and the secondary location at 493.5 nm.

[79] Figures 13b and 13c show examples of spectra from Mars targets with various amounts of Ti, Si, and Ba. Stark is high in SiO_2 (>60 wt %) and low TiO_2 (<1 wt %) while Thor_Lake point five is high in TiO_2 (>3 wt %) and low in SiO_2 (<40 wt %) [*Sautter et al.*, 2013]. Because the Si peak

at 455.4 nm has a slight bump on its right shoulder, it appears that Ba is present in Stark, and both PLS and univariate models estimate ~600 ppm Ba. However, as was shown in the modeling section, both models can be influenced by the presence of a large Si/Ti peak. But due to the slight asymmetry of the peak and a possible feature at 493.5 nm (Figure 13c), 600 ppm of Ba is reasonable. Preble point two (not shown) is similar to Stark and also has high estimated Ba (600–1000 ppm). There appears to be no detectable Ba in Thor_Lake point five. The other two examples, JakeM_1 point four and Akaitcho point seven, have mid-range abundances of Si and Ti. JakeM_1 point four likely has some Ba due to the slight "filling-in" of the dip between the Si/Ti peak and the rightmost Ti peak. The clearest detection of Ba in the first 100 sols is seen in Akaitcho point seven. While both Si and Ti peaks are present in the 455 nm region, the primary peak in this region is from Ba, and there is clearly a Ba peak at 493.5 nm. Lastly, several locations in Link show increased Ba (up to ~300 ppm) but the presence of the Si/Ti peak makes it very difficult to draw any conclusions from this observation.

[80] Focusing on the clearest detection of Ba, Akaitcho is a small accumulation of sand (and dust) that was analyzed as a ChemCam 3 × 3 grid taken on sol 50 of the traverse. Thirty shots were taken at each point. Inspection of the shot-to-shot signal intensity behavior suggests the laser is primarily striking unconsolidated material up to shot ~13 and shots 14–24 primarily struck a more solid material [*Meslin et al.*, 2013].
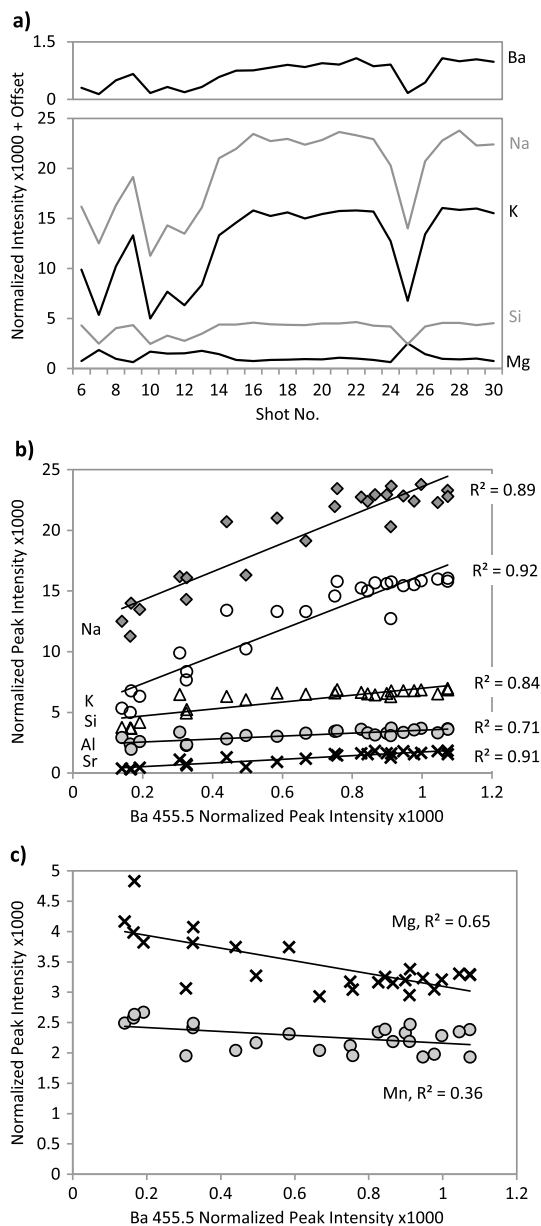
Figure 16. Peak intensity analysis of Ba in the Akaitcho sand ripple, point 7. (a) Ba peak intensity with depth compared to Na, K, Si, and Mg peak intensities. Increased Ba, Na, K, and Si are posited to correspond to a buried pebble. (b) Peak intensities for Si, Na, K, Si, Al, and Sr correlate positively with Ba while (c) Mg and Mn correlate inversely. Some peaks have been scaled; plotted here are Na 589 nm, K 767 nm, Si 635 nm (×1.5), Al 705 (×5), Sr 422 nm (×6), Mg 518 nm, and Mn 403 nm (×10). Note that intensities are not representative of absolute abundance. For major elements, smaller peaks are chosen because they are less susceptible to saturation and self-absorption.

The latter shots are coincident to the spectra enriched in Ba (Figure 16a). Several elements, including Na, K, Si, Al, and Sr, correlate strongly with Ba (Figure 16b) while Mg and Mn have weaker negative correlations with Ba (Figure 16c). Using Ba and the alkalis as a signature for the pebble, a plausible scenario to explain the behavior of the depth profile

is that the laser is slowly exhuming the pebble, and a portion of the pebble is sampled by shot eight. Occasionally, sand falls back over the pebble as indicated by the dips in Ba and alkalis over shots 10–13 and 25. Estimates of Ba abundance from the averaged spectrum excluding the first five shots are 670 ppm (univariate) and 570 ppm Ba (PLS). To more accurately estimate the Ba in the pebble and soil, five single shot spectra at two locations corresponding to the high Ba regions (shots 16–20 and shots 26–30) were averaged and the peaks in the Ba region were fit for estimation in the univariate model. The averages of shots 16–20 and 26–30 estimate 855 ppm Ba and 991 ppm Ba, respectively, ~200–300 ppm more than in the averaged spectrum. For comparison, the very first shot over the profile predicts a negative value and the average of shots 2–5 is 65 ppm Ba.

[81] Terrestrial studies have shown Ba abundances follow Si in mafic compositions when olivine ± pyroxene ± plagioclase ± amphibole are crystallizing, but it decreases with increasing Si when K-feldspar, feldspathoids ± micas crystallize. Because Ba in Akaitcho point seven is correlated positively to Na, K, Si, and Al, an interpretation of the pebble as a feldspar or possibly a mica is reasonable. Concentrations of 800 to 1000 ppm of Ba are not uncommon in terrestrial feldspars and Ba-rich feldspars have been identified by *Hewins et al.* [2013] in the Martian breccia NWA 7533.

5.4. Rubidium and Strontium

[82] The targets within the first 100 sols that have the highest Rb also have the highest Sr and therefore we discuss these two elements together. These measurements provide the first detectable levels of Rb on Mars. The RMSEP for the PLS model used to calculate the following averages is 30 ppm for Rb and 160 ppm for Sr. The average abundance is ~25 ppm for the sand and soils and ~35 ppm for rocks and pebbles, including Link; these compare favorably to the estimates of 25 ppm and 56 ppm, respectively, made by *Brückner et al.* [2003] using Pathfinder K measurements and an SNC meteorite K/Rb ratio of 230. *Taylor and McLennan* [2009] estimate 12.5 ppm Rb in the bulk Martian crust, slightly lower than the observed Rb abundances, but the observed abundances are biased slightly toward higher concentrations due to an approximate detection limit of ~20 ppm. The average Sr abundance in rocks and pebbles is ~185 ppm, lower than *Brückner et al.*'s [2003] estimate of 405 ppm. For soils, the average observed Sr abundance is ~95 ppm, which is also lower than *Brückner et al.*'s [2003] estimate of 189 ppm Sr.

[83] The most unique points for Sr and Rb are the five analysis points in Link, the conglomerate described by *Williams et al.* [2013], which have Rb >100 ppm and Sr >1000 ppm. Points two and three in the soil target Beaulieu appear to have struck loose pebbles and these pebbles have Rb > 100 ppm and Sr > 500 ppm. Three points in rocks have Rb between 60 and 80 ppm: sol 22 Preble point two, sol 48 JakeM_1 point five, and sol 32 Taltheilei point four, which also has Sr > 400 ppm. There are midrange Rb abundances in a buried pebble at point two in the sol 49 Anton soil, which has ~60 ppm Rb, and point two in the Akaitcho sand accumulation, which has ~65 ppm Rb. Additionally, there are several targets that have Sr > 400 ppm: sol 22 Murky point two (pebble in soil), sol 32 Taltheilei points one, four, and five (bedrock); sol 43 Kam point five

(pebble in soil); and sol 45 Jake_M point three (float rock). Table 4 provides summary statistics for Rb and Sr within each material type for all targets within the first 100 sols. The means of Rb and Sr for all categories except for Link are within the models' RMSEPs. Major element abundances associated with these points are presented in Table 5 and spectra of the Rb and Sr for these points are shown in Figures 13d and 13e. For comparison, several targets with low Rb and/or Sr abundances are also plotted (Portage soil and Coronation or Jake_M).

[84] Link is very high in both Rb and Sr, and we have attempted to identify possible Rb- and Sr-bearing minerals based on the elements they correlate with. In *Williams et al.* [2013], the light-toned clasts are interpreted to be feldspar grains and the cementing matrix appears to be enriched in Fe, Ti, and Cr. This is primarily based on an observation of a pronounced change in composition with depth over the 50 shots taken on the fifth point on Link in which material enriched in Fe, Ti, and Cr is ablated revealing a composition beneath that is similar to the other four locations, enriched in Si, K, Na, and Ca. Figures 17a–17c show this compositional change clearly for Ca, Na and Fe relative to Si. The surface shots for point five (beginning after the first five shots) start on the left side of the plots (low Si) and Ca and Na increase in concentration with depth toward the composition of the other four locations and Fe decreases with depth.

[85] While the changes with depth for major elements are quite clear, determining the relation between Sr and Rb and the major elements is less clear. For Sr in point five (Figures 17d–17f), there appears to be a complex relationship where Sr appears to initially increase, decrease and then increase again once in the putative feldspar grain. This "sawtooth" like pattern appears in plots of Sr with Si, Ca, Al, Na, Ti, and Fe, although it is only apparent in Al after thorough inspection of the peak intensities. This may be explained by variable sampling initially of the Fe-rich material relative to the underlying Si-rich clasts, and matrix effects between the components may disproportionately affect Sr emission. This would indicate Sr predominately resides in the Si-rich clasts. However, if matrix effects are not a factor, it may indicate that Sr is present in both materials. Focusing on the Al and Ca versus Sr plots, possible trends are revealed between the first four analysis points and shots 30–50 of point five. Al and Sr are correlated positively and it appears that Ca and Sr are correlated negatively.

[86] Rb is more difficult to analyze due to its primary peak's position near the large O peak. In Link point five, the Fe-rich material has a larger O peak than the underlying material and the O 777 nm peak intensity decreases by 12.5% from the average of shots 6–10 relative to shots 46–50. This decrease in O peak intensity is mimicked in Rb where the percent change with depth between the Rb peak intensity over the average of shots 6–10 and shots 46–50 is 23%. The drop in the O peak intensity is a matrix effect that is affecting the Rb peak intensity and thus Rb abundances also appear to decrease with depth.

[87] However, earlier results presented in the supplementary material of *Williams et al.* [2013] pointed toward Rb increasing with depth in point five, and thereby implying the Rb is associated with the putative feldspar clasts. That interpretation was based on a different normalization scheme in which the spectra were normalized to the total emission across all spectrometers

instead of the total emission for each spectrometer. There is a 70% decrease in the UV spectral range total emission from the first shots on the Fe-rich matrix (shots 6–10) to the shots predominately in the Si-rich matrix (shots 35–40) and this significantly influences the sum of the total emission across all spectrometers. The VNIR spectrometer, in which the Rb and O peaks are present, only decreases by 13% over the same range. The drastic change in total emission in the UV is likely due to the large number of Fe and Ti lines in that region and these peaks decrease in size as the Fe-Ti rich component is ablated, thus reducing the total emission. After normalization to the total emission, Rb appears to increase with depth, and thus associated with Si, K, Na, and Ca. This is in opposition to results obtained with data normalized to each spectrometer's total emission and, therefore, observations of changes in Rb in point five are difficult to interpret due to opposing results obtained from different normalization schemes. This is an extreme case study in which highly different chemical matrices are sampled in a depth profile and it highlights the importance of normalization.

[88] Examination of three of the other locations on Link reveals that points one, three, and four do not show a significant compositional change with depth and the O peak intensity and total emission are relatively consistent over shots 6–50. Therefore it may be possible to determine if there is a correlation between Rb and any other major elements with minimal influence from matrix effects in these points (Figures 17g and 17h). Because there are no significant changes with depth, we cannot rely on shot-to-shot variability and therefore we look at the trend formed by all points. In this case, there appears to be a positive correlation between Al, K, and Sr with Rb when the three locations are taken together. This provides some evidence for Rb being associated with the suggested feldspar phase.

[89] Given the complexities associated with the total emission, the variability in the intensity of the O peaks, the potential matrix effects between a Fe-rich matrix and a Si-matrix, and how each of these factors affect the chosen normalization procedure, it is very difficult to interpret the behavior of Rb in Link point five without additional laboratory work exploring these issues on a sample of known composition. At this time, the best evidence that Rb and Sr are present in the Si-rich material is that all five locations show consistently high Rb and Sr and, from the RMI imagery, these locations appear to have struck light-toned clasts. The Si-rich material is associated with high Al, K, Na, and Ca, and thus consistent with a feldspar interpretation. This interpretation does not exclude Rb and/or Sr being present in the Fe-rich matrix material as well because all shots in the 50-shot depth profile on Link point five contain significant amounts of Rb and Sr. It is possible that the initial shots sampled only Fe-rich matrix material, thus implying Rb and Sr are present in the cement. It is also possible that all shots sampled some portion of the Fe-rich matrix and the Si-rich clasts. Additional data on Link-like conglomerates would be required to further constrain the composition of the matrix.

[90] Examination of the high Sr and Rb points in the Beaulieu pebbles, Taltheilei, and Jake_M shows no significant changes with depth and therefore shot-to-shot studies are not productive in understanding element correlations. However, these locations tend to have high Si and alkalis contents (Table 5), consistent with Link and a feldspar interpretation,
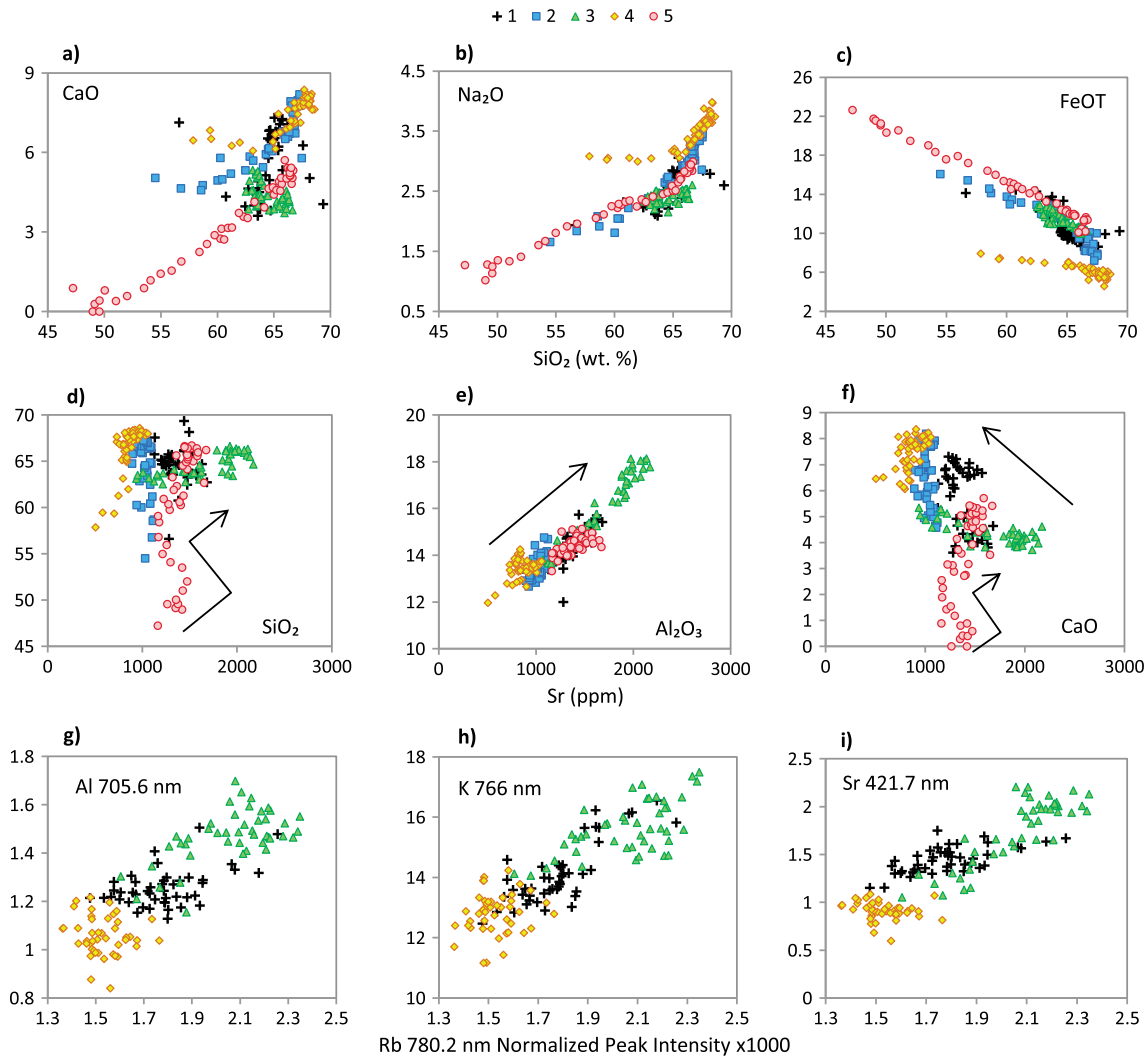
Figure 17. Variation diagrams for the 5 analysis points on Link. Major element PLS abundances (wt %) for (a) CaO (RMSEP 4.2 wt %), (b) Na$_2$O (RMSEP 0.7 wt %), and (c) FeOT (RMSEP 3.2 wt %) plotted against SiO$_2$ (RMSEP 7.3 wt %) illustrating the change in depth that occurs in point five of Link and to a lesser extent in points two and four. Major element PLS abundances for (d) SiO$_2$, (e) Al$_2$O$_3$ (RMSEP 3.9 wt %), and (f) CaO (RMSEP 4.2 wt %) plotted against Sr (RSMEP 160 ppm) demonstrate the unusual trends observed in point five for Si and Ca. The positive correlation between points for Al$_2$O$_3$ with Sr and the inverse correlation with Ca are also indicated. Plots show the positive correlation between Rb normalized peak intensities ×1000 and (g) Al, (h) K, and (i) Sr normalized peak intensities ×1000 for points one, three, and four, which showed the least influence from the nearby O peak.

and in the case of Jake_M, this is also consistent with the results from APXS, where the whole rock chemistry implied a high fraction of feldspar [*Stolper et al.*, 2013].

[91] K versus Rb plots and K/Rb ratios are often used to make inferences about magmatic fractionation processes, as well as about weathering and metasomatism. Figure 18 shows a plot of Rb and K with outlines of the regions for the different material types encountered in the traverse. For reference, generalized fields of several rock types and minerals are shown. Also plotted are estimates of the terrestrial K/Rb ratios for the continental crust (296) and for depleted mid-ocean ridge basalts (MORB, 1071) [*McDonough et al.*, 1992]. The median % K obtained from the gamma ray spectrometer (GRS) for the Gale crater region (~0.33 ± 0.03% K) from *Gasnault et al.* [2010] is plotted as a horizontal line

across the chart. The majority of ChemCam points fall between the terrestrial continental crust fractionation line and the depleted MORB estimates and the error bars typically encompass both lines. Most of the rocks, soils, and sand fall in the general mafic/intermediate rock field and partially overlap the upper ranges of the SNC meteorite and pyroxene fields. The exceptions to these observations are the high Rb points in Link and two Beaulieu pebbles which fall below the continental crust line and the Rb and K error bars do not encompass it. These points lie below the high K/high Rb terrestrial data plotted here (granites and rhyolites (felsic)/illite-smectite/K-feldspar). K abundances from APXS plotted with ChemCam Rb abundances occupy the same space as ChemCam data, indicating consistency between the two techniques for K; Rb was not detected by APXS in Jake_M.
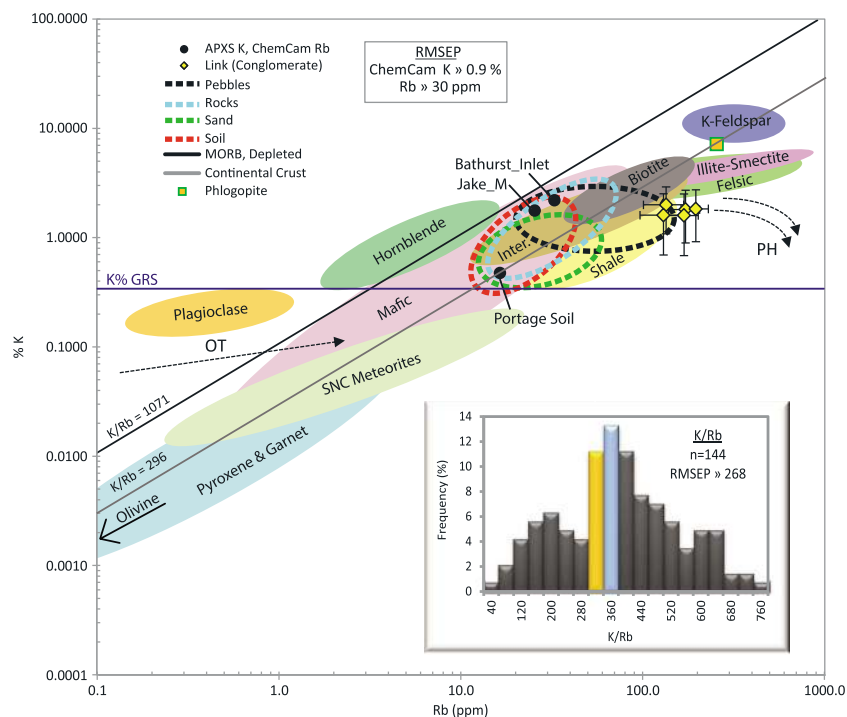
Figure 18. Rb versus K plot showing the Gale crater data relative to major rock types, minerals, and the SNC meteorites. Terrestrial K/Rb ratios for mid-ocean ridge basalts (MORB) and the continental crust are from *McDonough et al.* [1992]. Percent K from GRS, represented by a horizontal line, is the median for the Gale region (0.33 % K ± 0.03) [*Gasnault et al.*, 2010]. The data from Gale crater generally lie on the main terrestrial fractionation trend described by *Shaw* [1968], which approximately corresponds to the continental crust K/Rb line. The pegmatitic-hydrothermal (PH) and the oceanic theoleitic (OT) trends from *Shaw* [1968] are indicated with dashed lines; Gale materials do not follow these trends. Inset: Frequency histogram of K/Rb ratios in percent. The orange bar is the 280–320 bin, which contains the bulk crust K/Rb estimate (300) from *Taylor and McLennan* [2009] and the blue bar is the 320–360 bin, which contains the K/Rb ratio (344) obtained from the average of 17 SNC meteorite whole rock compositions. The highest percent of ChemCam data lies within or near these ratios bins. Reference data fields are based on values given in the following sources (BSI refers to standards in the Brammer's Standard Inc. collection): plagioclase (*n* = 56) [*Kinman et al.*, 2009], pyroxene (*n* = 21) [*Griffin and Rama Murthy*, 1969], garnet (*n* = 12) [*Griffin and Rama Murthy*, 1969], olivine (*n* = 5) [*Griffin and Rama Murthy*, 1969], shale (*n* = 29 [*Wronkiewicz and Condie*, 1987] 6 from BSI), mafic (*n* = 96 [*Choi et al.*, 2013; *Dostal et al.*, 1991; *Jafri and Sheikh*, 2013; *Perez et al.*, 2013; *Xu et al.*, 2012; *Taylor et al.*, 1956; *Sarifakioğlu et al.*, 2013; *Gast* 1965] and 14 from BSI), hornblende (*n* = 4) [*Griffin and Rama Murthy*, 1969], intermediate (inter., *n* = 15 [*Choi et al.*, 2013; *Taylor et al.*, 1956] and 7 from BSI), illite-smectite (*n* = 15) [*Gilg et al.*, 2003; *Saleemi and Ahmed*, 2000], felsic (*n* = 57 [*Zhang et al.*, 2011; *Alirezaei and Hassanzadeh*, 2012; *Huang et al.*, 2012; *Kaygusuz et al.*, 2012; *Caffe et al.*, 2012; *Taylor et al.*, 1956] and 10 from BSI), phlogopite (*n* = 1) [*Griffin and Rama Murthy*, 1969], K-feldspar (*n* = 40 [*Huntley and Hancock*, 2001; *Wilson and Coats*, 1972] and 2 from BSI), and SNC meteorites (*n* = 17) [*Barrat and Bollinger*, 2010; *Filiberto et al.*, 2012 and references therein; *McSween*, 2003].

[92] Based on the igneous fractionation trends described in *Shaw* [1968], these data are broadly consistent with the "main trend" observed in terrestrial materials, which roughly corresponds to the K/Rb continental crust line in Figure 18. The oceanic theoleitic basaltic trend (OT) is located in the direction of the plagioclase field while the pegmatitic-hydrothermal (PH) trend is located in the upper right side of the plot. Highly weathered samples would lie to the lower right of the main trend due to the preferential retention of Rb over K as clay minerals are formed [e.g., *Nesbitt et al.*, 1980]. While Link and several pebbles appear to lie below this main trend, neither the K nor Rb estimates are accurate enough at this time to determine if this trend is due to weathering

processes or is simply an underestimation of K or an overestimation of Rb.

[93] A frequency histogram of K/Rb ratios is inset in Figure 18. The most commonly occurring ratio range is 320–360, which encompasses the average value calculated from 17 SNC meteorite bulk measurements, 344 (range 150 to 770). The next most frequent ratio range (280–320) from ChemCam data includes the estimated ratio from *Taylor and McLennan*, [2009] of 299.2. The broad correspondence between observations from ChemCam, the SNC meteorites, and modeled estimates suggests that our measurements are reflecting a widespread compositional trend in Martian materials. The large range of ratios in the ChemCam data set

is likely a result of the small analysis spot size which may sample individual grains; there may also be a small number of outliers resulting from anomalous K or Rb estimates.

6. APXS Trace Element Results

[94] Preliminary Rb, Sr, and Ba trace element concentrations for three rocks, Jake_M, Bathurst_Inlet, and Et Then, and one soil, Portage, were analyzed by fitting the APXS spectra using the computer code GUAPX. No Rb or Ba detections were made in any sample. All three Sr determinations by GUAPX lay between the limit of detection (LOD) and the limit of quantitation (LOQ), the latter term referring to the level at which quantitative discussion of the result is justified. The values given by GUAPX for LOD and LOQ are, respectively, ~100 ppm and ~300 ppm. Work continues to refine the modeling of the overlap between Rb and Sr peaks and the Pu L X-ray scatter peaks which are largely responsible for determining the detection limits. Jake_M and Portage were analyzed by ChemCam, but Et Then was not. The estimated Sr abundance range determined by APXS for Jake_M and Portage compare favorably to ChemCam estimates. In Jake_M, the average of nine ChemCam observation points with positive estimates is 100 ppm and in Portage, the average is 70 ppm over five points with positive estimates (RMSEP for Sr = 160 ppm).

7. Conclusions

[95] The trace element results for ChemCam provide the first in situ measurements of Li and Ba, the highest in situ observation of Sr, and the first detectable abundance of Rb on Mars. Univariate and PLS models have been developed for quantifying these elements. This modeling is preliminary and work is underway to supplement the training set to more accurately represent the compositional ranges observed at Gale crater on Mars, and additional multivariate techniques are being tested to improve accuracy. The major findings observed in the first 100 sols from the Bradbury Landing Site to the Rocknest location are the following:

[96] 1. Li is low in the majority of rocks and soils, as expected for dominantly basaltic materials. If the salt component of the soils identified by Viking and subsequent missions was formed via precipitation from fluids derived from extensive hydrothermal processes, then Li concentrations should be enriched in the soils. Instead, it appears that the Li abundance fits the vapor-transport mechanisms for enriching the soil in S and Cl.

[97] 2. Several LIBS points in rocks have Li > 30 ppm and may imply the presence of primary igneous phases enriched in Li or secondary minerals such as clays.

[98] 3. Bathurst_Inlet is enriched in Li and several locations show a marked decrease in Li with depth. This trend is associated with Rb, Na, and K, and the surface enrichment in these elements is interpreted to be due to aqueous alteration processes (i.e., frost deposition, followed by melt and evaporation or sublimation) that have preferentially mobilized the alkalis.

[99] 4. Up to ~1000 ppm Ba has been observed in a buried pebble in the Akaitcho sand ripple. The Ba is associated with Si, Na, and K, indicating it may be present in an alkali feldspar grain.

[100] 5. Rb and Sr are present at high abundances (>100 ppm and >1000 ppm, respectively) in the conglomerate Link. Additional locations with Rb >50 ppm and Sr >500 ppm have been identified in several rocks and pebbles. The majority of these locations also have high SiO_2 (>60 wt %), high alkali abundances (>4 wt % $Na_2O + K_2O$), consistent with a feldspathic composition.

[101] 6. Sr estimates in Portage and Jake_M are consistent (within error) between ChemCam and APXS.

[102] 7. Trends in K with Rb show that the data obtained in Gale crater follow the main fractionation trend established by *Shaw* [1968] and there is no evidence for significant weathering from the ratio of these two elements.

[103] Overall, the trace element data presented here provide additional evidence for magmatic differentiation [e.g., *Sautter et al.*, 2013; *Stolper et al.*, 2013] and potentially for a small amount of surface aqueous alteration on Mars.

References

Agee, C. B., et al. (2013), Unique meteorite from early Amazonian Mars: Water-rich basaltic breccia Northwest Africa 7034, *Science*, *339*, 780–785.

Alirezaei, S., and J. Hassanzadeh (2012), Geochemistry and zircon geochronology of the Permian A-type Hasanrobat granite Sanandaj-Sirjan belt: A record of the Gondwana break-up in Iran, *Lithos*, *151*, 122–134.

Anderson, R. B., and J. F. Bell III (2010), Geologic mapping and characterization of Gale crater and implications for its potential as a Mars Science Laboratory landing site, *Mars*, *5*, 76–128.

Anderson, R. B., R. V. Morris, S. M. Clegg, J. F. Bell III, R. C. Wiens, S. D. Humphries, S. A. Mertzman, T. G. Graff, and R. McInroy (2011), The influence of multivariate analysis methods and target grain size on the accuracy of remote quantitative chemical analysis of rocks using laser-induced breakdown spectroscopy, *Icarus*, *215*, 608–627.

Anderson, R. B., J. F. Bell III, R. C. Wiens, R. V. Morris, and S. M. Clegg (2012), Clustering and training set selection methods for improving the accuracy of quantitative laser induced breakdown spectroscopy, *Spectrochim. Acta B*, *70*, 24–32, doi:10.1016/j.sab.2012.04.004.

Anzano, J. M., M. A. Villoria, A. Ruíz-Medina, and R. J. Lasheras (2006), Laser-induced breakdown spectroscopy for quantitative spectrochemical analysis of geological materials: Effects of the matrix and simultaneous determination, *Anal. Chim. Acta*, *575*, 230–235.

Bandfield, J. L., V. E. Hamilton, P. R. Christensen, and H. Y. McSween Jr. (2004), Identification of quartzofeldspathic materials on Mars, *J. Geophys. Res.*, *109*, E10009, doi:10.1029/2004JE002290.

Banin, A., F. X. Han, I. Kan, and A. Cicelsky (1997), Acidic volatiles and the Mars soil, *J. Geophys. Res.*, *102*, 13,341–13,356.

Barrat, J.-A., and C. Bollinger (2010), Geochemistry of the Martian meteorite ALH 84001, revisited, *Meteorit. Planet. Sci.*, *45*, 495–512.

Barrat, J.-A., A. Jambon, M. Bohn, P. Gillet, V. Sautter, C. Gopel, M. Lesourd, and F. Keller (2002), Petrology and chemistry of the Picritic Shergottite North West Africa 1068 (NWA 1068), *Geochim. et Cosmochim. Acta*, *66*, 3505–3518.

Beck, P., J. A. Barrat, M. Chaussidon, P. Gillet, and M. Bohn (2004), Li isotopic variations in single pyroxenes from the Northwest Africa 480 shergottite (NWA 480): A record of degassing of Martian magmas?, *Geochim. et Cosmochim. Acta*, *68*, 2925–2933.

Beck, P., M. Chaussidon, J. A. Barrat, P. H. Gillet, and M. Bohn (2006), Diffusion induced Li isotopic fractionation during the cooling of magmatic rocks: The case of pyroxene phenocrysts from nakhlite meteorites, *Geochim. et Cosmochim. Acta*, *70*, 4813–4825.

Bish, D. L., et al. (2013), X-ray diffraction results from Mars Science Laboratory: Mineralogy of Rocknest Aeolian bedform at Gale crater, *Science*, *341*, doi:10.1126/science.1238932.

Blake, D. F., et al. (2013), Curiosity at Gale crater, Mars: Characterization and analysis of the Rocknest sand shadow, *Science*, *341*, doi:10.1126/science.1239505.

Borg, L. E., and D. S. Draper (2003), A petrogenetic model for the origin and compositional variation of the Martian basaltic meteorites, *Meteorit. Planet. Sci.*, 38, 1713–1731.

Borg, L. E., L. E. Nyquist, L. A. Taylor, H. Wiesmann, and C.-Y. Shih (1997), Constraints on Martian differentiation processes from Rb-Sr and Sm-Nd isotopic analyses of the basaltic shergottite QUE 94201, *Geochim. et Cosmochim. Acta*, 61, 4915–4931.

Borg, L. E., L. E. Nyquist, H. Wiesmann, and Y. Reese (2002), Constraints on the petrogenesis of Martian meteorites from the Rb-Sr and Sm-Nd isotopic systematics of the lherzolitic shergottites ALH77005 and LEW88516, *Geochim. et Cosmochim. Acta*, 66, 2037–2053.

Bousquet, B., J.-B. Sirven, and L. Canioni (2007), Towards quantitative laser-induced breakdown spectroscopy analysis of soil samples, *Spectrochim. Acta B*, 62, 1582–1589.

Bridges, J. C., and M. M. Grady (2000), Evaporite mineral assemblages in the nakhlite (Martian) meteorites, *Earth Planet. Sci. Lett.*, 176, 267–279.

Brückner, J., G. Dreibus, R. Rieder, and H. Wänke (2003) Refined data of Alpha Proton X-ray Spectrometer analyses of soils and rocks at the Mars Pathfinder site: implications for surface chemistry, *J. Geophys. Res.*, 108(E12), 8094, doi:10.1029/2003JE002060.

Bulajic, D., M. Corsi, G. Cristoforetti, S. Legnaioli, V. Palleschi, A. Salvetti, and E. Tognoni (2002), A procedure for correcting self-absorption in calibration free-laser induced breakdown spectroscopy, *Spectrochim. Acta B*, 57, 339–353.

Caffe, P. J., R. B. Trumbull, and W. Siebel (2012), Petrology of the Coyaguayma ignimbrite, northern Puna of Argentina: Origin and evolution of a peraluminous high-SiO$_2$ rhyolite magma, *Lithos*, 134–135, 179–200.

Campbell, J. L., M. Lee, B. N. Jones, S. M. Andrushenko, N. G. Holmes, and J. A. Maxwell (2009), A fundamental parameters approach to calibration of the Mars Exploration Rovers alpha-particle X-ray spectrometer, *J. Geophys. Res.*, 114, E04006, doi:10.1029/2008JE003272.

Campbell, J. L., S. Andrushenko, S. M. Taylor, and J. A. Maxwell (2010), A fundamental parameters approach to calibration of the Mars Exploration Rovers alpha-particle X-ray spectrometer. Part II. Unknown samples, *J. Geophys. Res.*, 115, E04009, doi:10.1029/2009JE003481.

Campbell, J. L., G. M. Perrett, R. Gellert, S. M. Andrushenko, N. I. Boyd, J. A. Maxwell, P. L. King, and C. D. M. Schofield (2012), Calibration of the Mars Science Laboratory alpha particle X-ray spectrometer, *Space Sci. Rev.*, 170, 319–340, doi:10.1007/s11214-012-9873-5.

Chan, L. H., J. M. Edmond, G. Thompson, and K. Gills (1992), Lithium isotopic composition of submarine basalts: Implications for the lithium cycle in the oceans, *Earth Planet. Sci. Lett.*, 108, 151–160.

Chennaoui Aoudjehane, H., et al. (2012), Tissint Martian meteorite: A fresh look at the interior surface, and atmosphere of Mars, *Science*, 338, 785–788.

Choi, H.-O., S. H. Choi, D.-C. Lee, and H.-C. Kang (2013), Geochemical evolution of basaltic volcanism within the tertiary basins of southeastern Korea and the opening of the East Sea (Sea of Japan), *J. Volcanol. Geotherm. Res.*, 249, 109–122.

Clark, B. C., and A. K. Baird (1979), Is the Martian lithosphere sulfur rich?, *J. Geophys. Res.*, 84, 8395–8402.

Clark, B. C., and D. C. Van Hart (1981), The salts of Mars, *Icarus*, 45, 370–378.

Clark, B. C., A. K. Baird, R. J. Weldon, D. M. Tsusaki, L. Schnabel, and M. P. Candelaria (1982), Chemical composition of Martian fines, *J. Geophys. Res.*, 87, 10,059–10,067.

Clegg, S. M., R. C. Wiens, J. E. Barefield, E. Sklute, and M. D. Dyar (2009), Quantitative remote laser-induced breakdown spectroscopy by multivariate analysis, *Spectrochim. Acta B*, 64, 79–88.

Cousin, A., O. Forni, S. Maurice, O. Gasnault, C. Fabre, V. Sautter, R. C. Wiens, and J. Mazoyer (2011), Laser induced breakdown spectroscopy library for the Martian environment, *Spectrochim. Acta B*, 66, 805–814.

Cremers, D. A., and L. J. Radziemski (2006), *Handbook of Laser-Induced Breakdown Spectroscopy*, John Wiley, Chichester, U.K.

Dostal, J., L. Toscani, A. Photiades, and S. Capedri (1991), Geochemistry and petrogenesis of Tethyan ophiolites from northern Argolis (Peloponnesus, Greece), *Eur. J. Mineral.*, 3, 105–121.

Dyar, M. D., J. M. Tucker, S. Humphries, S. M. Clegg, R. C. Wiens, and M. D. Lane (2010), Strategies for Mars remote laser-induced breakdown spectroscopy analysis of sulfur in geological samples, *Spectrochim. Acta B*, 66, 39–56, doi:10.1016/j.sab2010.11.016.

Dyar, M. D., M. L. Carmosino, E. A. Speicher, M. V. Ozanne, S. M. Clegg, and R. C. Wiens (2012), Comparison of partial least squares and LASSO regression techniques for laser-induced breakdown spectroscopy data of geological samples, *Spectrochim. Acta B*, 70, 51–67, doi:10.1016/j.sab.2012.04.011.

Eppler, A. S., D. A. Cremers, D. D. Hickmott, M. J. Ferris, and A. C. Koskelo (1996), Matrix effects in the detection of Pb and Ba in soils using laser-induced breakdown spectroscopy, *Appl. Spectrosc.*, 50, 1175–1181.

Essington, M. E., G. V. Melnichenko, M. A. Stewart, and R. A. Hull (2009), Soil metals analysis using laser-induced breakdown spectroscopy (LIBS), *SSSAJ*, 73, 1469–1478.

Fabre, C., M. C. Boiron, J. Dubessy, A. Chabiron, B. Charoy, and T. M. Crespo (2002), Advances in lithium analysis in solids by means of laser-induced breakdown spectroscopy: An exploratory study, *Geochim. et Cosmochim. Acta*, 66, 1401–1407.

Fabre, C., S. Maurice, A. Cousin, R. C. Wiens, O. Forni, V. Sautter, and D. Guillaume (2011), Onboard calibration igneous targets for the Mars Science Laboratory Curiosity rover and the Chemistry Camera laser induced breakdown spectroscopy instrument, *Spectrochim Acta B*, 66, 280–289.

Filiberto, J., E. Chin, J. M. D. Day, I. A. Franchi, R. C. Greenwood, J. Gross, S. C. Penniston-Dorland, S. P. Schwenzer, and A. H. Treiman (2012), Geochemistry of intermediate olivine-phyric shergottite Northwest Africa 6234, with similarities to basaltic shergottite Northwest Africa 480 and olivine-phyric shergottite Northwest Africa 2990, *Meteorit. Planet. Sci.*, 47, 1256–1273.

Garvie, L. A. J., D. M. Burt, and P. R. Buseck (2008), Nanometer-scale complexity, growth, and diagenesis in desert varnish, *Geology*, 36, 215–218.

Gasnault, O., G. J. Taylor, S. Karunatillake, J. Dohm, H. Newsom, O. Forni, P. Pinet, and W. V. Boynton (2010), Quantitative geochemical mapping of Martian elemental provinces, *Icarus*, 207, 226–247.

Gast, P. W. (1965), Terrestrial ratio of potassium to rubidium and composition of Earth's mantle, *Science*, 147, 858–860.

Gellert, R., et al. (2006), Alpha particle X-ray spectrometer (APXS): Results from Gusev crater and calibration report, *J. Geophys. Res.*, 111 E02S05, doi:10.1029/2005JE002555.

Gilg, H. A., B. Weber, J. Kasbohm, and R. Frei (2003), Isotope geochemistry and origin of illite-smectite and kaolinite from the Seilitz and Kemmlitz kaolin deposits Saxony, Germany, *Clay Miner.*, 38, 95–112.

Griffin, W. L., and V. Rama Murthy (1969), Distribution of K, Rb, Sr and Ba in some minerals relevant to basalt genesis, *Geochim. et Cosmochim. Acta*, 33, 1389–1414.

Grotzinger, J. P., et al. (2012), Mars Science Laboratory mission and science investigation, *Space Sci. Rev.*, 170, 5–56, doi:10.1007/s11214-012-9892-2.

Grotzinger, J. P., et al. (2013), A habitable fluvio-lacustrine environment at Yellowknife Bay, Gale crater, Mars, *Science*, doi:10.1126/science.1242777.

Haberle, R. M., et al. (2013), Preliminary interpretation of the REMS pressure data from the first 100 sols of the MSL mission, accepted with revisions to. *J Geophys. Res. Planets*, 119, 255–285, doi:10.1002/2013JE004517.

Herd, C. D. K., A. H. Treiman, G. A. McKay, and C. K. Shearer (2005), Light lithophile elements in Martian basalts: Evaluating the evidence for magmatic water degassing, *Geochim. et Cosmochim. Acta*, 69, 2431–2440.

Hewins, R. H., B. Zanda, M. Humayun, S. Pont, C. Fieni, and D. Deldicque (2013), Northwest Africa 7533, an impact breccia from Mars, *44th Lunar and Planetary Science Conference*, no. 1719.

Hilbk-Kortenbruck, F., R. Noll, P. Wintjens, H. Falk, and C. Becker (2001), Analysis of heavy metals in soils using laser-induced breakdown spectrometry combined with laser-induced fluorescence, *Spectrochim. Acta B*, 56, 933–945.

Horstman, E. L. (1957), The distribution of lithium, rubidium and caesium in igneous and sedimentary rocks, *Geochim. et Cosmochim. Acta*, 12, 1–28.

Huang, H., Z. Zhang, T. Kusky, M. Santosh, S. Zhang, D. Zhang, J. Liu, and Z. Zhao (2012), Continental vertical growth in the transitioinal zone between South Tianshan and Tarim, western Xinjiang, NW China: Insight from the Permian Halajun A1-type granitic magmatism, *Lithos*, 155, 49–66.

Huntley, D. J., and R. G. V. Hancock (2001), The Rb contents of the K-feldspar grains being measured in optical dating, *Ancient TL*, 19, 43–46.

Jafri, S. H., and J. M. Sheikh (2013), Geochemistry of pillow basalts from Bompoka, Andaman-Nicobar islands, Bay of Bengal, India, *J. Asian Earth Sci.*, 64, 27–37.

Johansson, S. A. E., and J. L. Campbell (1988), *PIXE: A Novel Technique for Elemental Analysis*, John Wiley, New York.

Kaygusuz, A. M., W. Arslan, F. S. Siebel, and N. Ilbeyli (2012), Geochronological evidence and tectonic significance of Carboniferous magmatism in the southwest Trabzon area, eastern Pontides, Turkey, *Int. Geol. Rev.*, 54, 1776–1800.

Kinman, W. S., C. R. Neal, J. P. Davidson, and L. Font (2009), The dynamics of Kerguelen Plateau magma evolution: New insights from major element, trace element and Sr isotope microanalysis of plagioclase hosted in Elan Bank basalts, *Chem. Geol.*, 264, 247–265.

Komsta, L. (2012), Chemometric and statistical evaluation of calibration curves in pharmaceutical analysis—A short review on trends and recommendations, *J. AOAC Int.*, 95, 669–672.

Kramida, A., Y. Ralchenko, J. Reader, and NIST ASD Team (2012) NIST atomic spectra database (version 5.0), [Online]. Available at http://physics.nist.gov/asd [Friday, 09 August 2013 14:52:40 EDT]. National Institute of Standards and Technology, Gaithersburg, Md.

Krasniker, R., B. Valery, and I. Schechter (2001), Study of matrix effects in laser plasma spectroscopy by shock wave propagation, *Spectrochim. Acta B*, *56*, 609–618.

Lasue, J., R. C. Wiens, S. M. Clegg, D. T. Vaniman, K. H. Joy, S. Humphries, A. Mezzacappa, N. Melikechi, R. E. McInroy, and S. Bender (2012), Remote laser-induced breakdown spectroscopy (LIBS) for lunar exploration, *J. Geophys. Res.*, *117*, E01002, doi:10.1029/2011JE003898.

Laville, S., M. Sabsabi, and F. R. Doucet (2007), Multi-elemental analysis of solidified mineral melt samples by laser-induced breakdown spectroscopy coupled with a linear multivariate calibration, *Spectrochim. Acta B*, *62*, 1557–1566.

Lazic, V., R. Barbini, F. Colao, R. Fantoni, and A. Palucci (2001), Self-absorption model in quantitative laser induced breakdown spectroscopy measurements on soils and sediments, *Spectrochim Acta B*, *56*, 807–820.

Lentz, R. C. F., H. Y. McSween Jr., J. Ryan, and L. R. Riciputi (2001), Water in Martian magmas: Clues from light lithophile elements in shergottite and nakhlite pyroxenes, *Geochim. et Cosmochim. Acta*, *65*, 4551–4565.

Leshin, L. A., et al. (2013), Volatile, isotope and organic analysis of Martian fines with the Mars Curiosity rover, *Science*, *341*, doi:10.1126/science.1238937.

Magna, T., U. Wiechert, and A. N. Halliday (2006), New constraints on the lithium isotope compositions of the Moon and terrestrial planets, *Earth Planet. Sci. Lett.*, *243*, 336–353.

Mahaffy, P. R., et al. (2013), Abundance and isotopic composition of gases in the Martian atmosphere from the Curiosity rover, *Science*, *341*, doi:10.1126/science.1237966.

Mansoori, A., B. Roshanzadeh, M. Khalaji, and S. H. Tavassoli (2011), Quantitative analysis of cement powder by laser-induced breakdown spectroscopy, *Optics Laser Eng.*, *49*, 318–323.

Martin, M. Z., S. Allman, D. J. Brice, R. C. Martin, and N. O. Andre (2012), Exploring laser-induced breakdown spectroscopy for nuclear materials analysis and in-situ application, *Spectrochim. Acta B*, *74–75*, 177–183.

Maurice, S., et al. (2012), The ChemCam instrument suite on the Mars Science Laboratory (MSL) rover: Science objectives and mast unit description, *Space Sci. Rev.*, doi:10.1007/s11214-012-9912-2.

Maxwell, J. A., W. J. Teesdale, and J. L. Campbell (1995), The Guelph PIXE software package II, *Nucl. Instr. Meth. B*, *95*, 407–421.

McDonough, W. F., and S.-S. Sun (1995), The composition of the Earth, *Chem. Geol.*, *120*, 223–253.

McDonough, W. F., S.-S. Sun, A. E. Ringwood, E. Jagoutz, and A. W. Hofmann (1992), Potassium, rubidium, and cesium in the Earth and Moon and the evolution of the mantle of the Earth, *Geochim. et Cosmochim. Acta*, *56*, 1001–1012.

McSween, H. Y., Jr. (2003), Mars, in *The Treatise on Geochemistry*, vol. 1, edited by H. D. Holland and K. K. Turekian, pp. 1–27, Elsevier Ltd, Oxford.

Meslin, P.-Y., et al. (2013), Soil diversity and hydration as observed by ChemCam at Gale crater, Mars, *Science*, *341*, doi:10.1126/science.1238670.

Mevik, B.-H., and R. Wehrens (2007), The pls package: Principal component and partial least squares regression in R, *J. Stat. Soft.*, *18*, 1–24.

Mezzacappa, A., N. Melikechi, A. Cousin, N. Lanza, S. Clegg, G. Berger, S. Bender, J. Lasue, R. Wiens, and S. Maurice (2013) On the effects of distance between a laser and its target in LIBS measurements, *FACSS Presents SciX*, no. 25.

Ming, D. W., et al. (2006), Geochemical and mineralogical indicators for aqueous processes in the Columbia Hills of Gusev crater, Mars, *J. Geophys. Res.*, *111*, E02S12, doi:10.1029/2005JE002560.

Morris, R. V., et al. (2006a), Mössbauer mineralogy of rock, soil, and dust at Gusev crater, Mars: Spirit's journey through weakly altered olivine basalt on the plains and pervasively altered basalt in the Columbia Hills, *J. Geophys. Res.*, *111*, E02S13, doi:10.1029/2005JE002584.

Morris, R. V., et al. (2006b), Mössbauer mineralogy of rock, soil, and dust at Meridiani Planum, Mars: Opportunity's journey across sulfate-rich outcrop, basaltic sand and dust, and hematite lag deposits, *J. Geophys. Res.*, *111*, E12S15, doi:10.1029/2006JE002791.

Morris, R. V., et al. (2008), Iron mineralogy and aqueous alteration from Husband Hill through Home Plate at Gusev Crater, Mars: Results from the Mössbauer instrument on the Spirit Mars Exploration Rover, *J. Geophys. Res.*, *113*, E12S42, doi:10.1029/2008JE003201.

Morris, R. V., et al. (2013), The amorphous component in Martian basaltic soil in global perspective from MSL and MER missions, *44th Lunar and Planetary Science Conference*, no. 1653.

Naes, T., T. Isaksson, T. Fearn, and T. Davies (2004), *A User-Friendly Guide to Multivariate Calibration and Classification*, NIR Publications, Chichester, U.K.

Nakamura, N. (1982), Origin and evolution of the Nakhla meteorite inferred from the Sm-Nd and U-Pb systematics and REE, Ba, Sr, Rb and K abundances, *Geochim. et Cosmochim. Acta*, *46*, 1555–1573.

Nath, B. N., K. Kunzendorf, and W. L. Plüger (2000), Influence of provenance, weathering, and sedimentary processes on the elemental ratios of the fine-grained fraction of the bedload sediments from the Vembanad lake and the adjoining continental shelf, southwest coast of India, *J. Sediment Res.*, *70*, 1081–1094.

Nesbitt, H. W., and R. E. Wilson (1992), Recent chemical weathering of basalts, *Am. J. Sci.*, *292*, 740–777.

Nesbitt, H. W., G. Markovics, and R. C. Price (1980), Chemical processes affecting alkalis and alkaline earths during continental weathering, *Geochim. et Cosmochim. Acta*, *44*, 1659–1666.

Newsom, H. E., and J. J. Hagerty (1997), Chemical components of the Martian soil: Melt degassing, hydrothermal alteration, and chondritic debris, *J. Geophys. Res.*, *102*, 19,345–19,355.

Newsom, H. E., J. Hagerty, and F. Goff (1999), Mixed hydrothermal fluids and the origin of the Martian soil, *J. Geophys. Res.*, *104*, 8717–8728.

Oldham, M. C., G. Konopka, K. Iwamoto, P. Langfelder, T. Kato, S. Horvath, and D. H. Geschwind (2008), Functional organization of the transcriptome in human brain, *Nat. Neurosci.*, *11*, 1271–1282.

Perez, A. d. C., D. V. Faustino-Eslava, G. P. Yumul Jr., C. B. Dimalanta, R. A. Tamayo Jr., T. F. Yang, and M.-F. Zhou (2013), Enriched and depleted characters of the Amnay Ophiolite upper crustal section and the regionally heterogeneous nature of the South China Sea mantle, *J. Asian Earth Sci.*, *65*, 107–117.

Pichavant, M., D. J. Kontak, L. Briqueu, J. V. Herrera, and A. H. Clark (1988), The Miocene-Pliocene Macusani volcanics SE Peru, Mineral, *Contrib. Mineral. Petrol.*, *100*, 325–338.

R Development Core Team n.d, R: A language and environment for statistical computing. R foundation for statistical computing, Vienna, Austria, ISBN 3-900051-07-0.

Rieder, R., H. Waenke, T. Economou, and A. Turkevich (1997), Determination of the chemical composition of Martian soil and rocks: the alpha proton X-ray spectrometer, *J. Geophys. Res.*, *102*, 4027–4044.

Rieder, R., R. Gellert, J. Brückner, G. Klingelhöfer, G. Dreibus, A. Yen, and S. W. Squyres (2003), The new Athena alpha particle X-ray spectrometer for the Mars Exploration Rovers, *J. Geophys. Res.*, *108*(E12), 8066, doi:10.1029/2003JE002150.

Rudnick, R. L., and S. Gao (2003), Composition of the continental crust, in *The Treatise on Geochemistry*, vol. 3, edited by H. D. Holland and K. K. Turekian, Elsevier Ltd, Chichester, U.K.

Ruzicka, A., G. A. Snyder, and L. A. Taylor (2001), Comparative geochemistry of basalts from the moon, earth, HED asteroid, and Mars: Implications for the origin of the moon, *Geochim. et Cosmochim. Acta*, *65*, 979–997.

Saleemi, A. A., and Z. Ahmed (2000), Mineral and chemical composition of Karak mudstone, Kohat Plateau, Pakistan: Implications for smectite-illitization of provenance, *Sediment. Geol.*, *130*, 229–247.

Sarifakioğlu, E., Y. Dilke, and J. A. Winchester (2013), Late Cretaceous subduction initiation and Palaeocene-Eocene slab breakoff magmatism in South-Central Anatolia, Turkey, *Int. Geol. Rev.*, *55*, 66–87.

Sautter, V., et al. (2013), Igneous mineralogy at Bradbury rise: The first ChemCam campaign, *J. Geophys. Res. Planets*, *119*, 30–46, doi:10.1002/2013JE004472.

Schmidt, M. E., et al. (2013), Geochemical diversity in first rocks examined by the Curiosity rover in Gale crater: Evidence for and significance of an alkali and volatile-rich igneous source, *J. Geophys. Res. Planets*, doi:10.1002/2013JE004481.

Shaw, D. M. (1968), A review of K-Rb fractionation trends by covariance analysis, *Geochim. et Cosmochim. Acta*, *32*, 573–601.

Speicher, E. A., M. D. Dyar, M. L. Carmosino, S. M. Clegg, and R. C. Wiens (2011), Single variable and multivariate analysis of remote laser-induced breakdown spectra for prediction of Rb, Sr, Cr, Ba and V in igneous rocks, *42nd Lunar and Planetary Science Conference*, no. 2385.

Stolper, E. M., et al. (2013), The petrochemistry of Jake_M: A Martian mugearite, *Science*, *341*, doi:10.1126/science.1239463.

Su, B.-X., H.-F. Zhang, E. Deloule, P. A. Sakyi, Y. Xiao, Y.-J. Tang, Y. Hu, J.-F. Ying, and P.-P. Liu (2012), Extremely high Li and low δ7Li signatures in the lithospheric mantle, *Chem. Geol.*, *292–293*, 149–157.

Taylor, S. R. and S. McLennan (2009) *Planetary Crusts: Their Composition, Origin and Evolution*, Cambridge Univ. Press, Cambridge, U.K., doi:10.1017/CB09780511575358.

Taylor, S. R., C. H. Emeleus, and C. S. Exley (1956), Some anomalous K/Rb ratios in igneous rocks and their petrological signficiance, *Geochim. et Cosmochim. Acta*, *10*, 224–229.

Tokar, R. L., et al. (2013), Searching for chemical variation across the surface of "Rocknest_3" using MSL ChemCam spectra, *42nd Lunar and Planetary Science Conference*, no. 1283.

Tomascak, P. B., C. H. Langmuir, P. J. le Roux, and S. B. Shirey (2008), Lithium isotopes in global mid-ocean ridge basalts, *Geochim. et Cosmochim. Acta*, *72*, 1626–1637.

Toulmin, P., III, A. K. Baird, B. C. Clark, K. Keil, H. J. Rose Jr., R. P. Christian, P. H. Evans, and W. C. Kelliher (1977), Geochemical and mineralogical interpretation of the Viking inorganic chemical results, *J. Geophys. Res.*, *82*, 4625–4634.

Tucker, J. M., M. D. Dyar, M. W. Schaefer, S. M. Clegg, and R. C. Wiens (2010), Optimization of laser-induced breakdown spectroscopy for rapid geochemical analysis, *Chem. Geol.*, *277*, 137–148.

Van Grieken, R. E., and A. A. Markowicz (1993), *Handbook of X-ray Spectroscopy: Methods and Techniques*, Marcel Dekker, Inc., New York.

Vaniman, D., M. D. Dyar, R. C. Wiens, A. Ollila, N. Lanza, J. Lasue, M. Rhodes, and S. M. Clegg (2012), Ceramic ChemCam calibration targets on Mars Science Laboratory, *Space Sci. Rev.*, *170*, 229–255, doi:10.1007/s11214-012-9886-0.

Velbel, M. A., D. T. Long, and J. L. Gooding (1991), Terrestrial weathering of Antarctic stone meteorites: Formation of Mg-carbonates on ordinary chondrites, *Geochim. et Consmochim. Acta*, *55*, 67–76.

Vigier, N., A. Decarreau, R. Millot, J. Carignan, S. Petit, and C. France-Lanord (2008), Quantifying Li isotope fractionation during smectite formation and implications for the Li cycle, *Geochim. et Cosmochim. Acta*, *72*, 780–792.

Wiens, R. C., et al. (2012), The ChemCam instrument suite on the Mars Science Laboratory (MSL) rover: Body unit and combined systems tests, *Space Sci. Rev.*, doi:10.1007/s11214-012-9902-4.

Wiens, R. C., et al. (2013), Pre-flight calibration and initial data processing for the ChemCam Laser-Induced Breakdown Spectroscopy (LIBS) instrument on the Mars Science Laboratory (MSL), *Spectrochim. Acta B*, *82*, 1–27, doi:10.1016/j.sab.2013.02.003.

Williams, R. M. E., et al. (2013), Martian fluvial conglomerates at Gale crater, *Science*, *340*, 1068–1072.

Wilson, J. R., and J. S. Coats (1972), Alkali feldspars from part of the Galway granite Ireland, *Mineral. Mag.*, *38*, 801–810.

Wronkiewicz, D. J., and K. C. Condie (1987), Geochemistry of Archean shales from the Witwatersrand Supergroup South Africa: Source-area weathering and provenance, *Geochim. et Cosmochim. Acta*, *51*, 2401–2416.

Wronkiewicz, D. J., and K. C. Condie (1990), Geochemistry and mineralogy of sediments from the Ventersdorp and Transvaal Supergroups, South Africa: Cratonic evolution during the early Proterozoic, *Geochim. et Cosmochim. Acta*, *54*, 343–354.

Xu, Y.-G., H.-H. Zhang, H.-N. Qiu, W.-C. Ge, and F.-Y. Wu (2012), Oceanic crust components in continental basalts from Shuangliao, Northeast China: Derived from the mantle transition zone?, *Chem. Geol.*, *328*, 168–184.

Yen, A. S., et al. (2005), An integrated view of the chemistry and mineralogy of Martian soils, *Nature*, *436*, 49–54, doi:10.1038/nature03637.

Yen, A. S., et al. (2013), Evidence for a global Martian soil composition extends to Gale crater, *44th Lunar and Planetary Science Conference*, Abs. No. 2495.

Zhang, Y., L. S. Shu, and X. Y. Chen (2011), Geochemistry, geochronology, and petro-genesis of the early Paleozoic granitic plutons in the central-southern Jiangxi Province, China, *Sci. China Earth*, *54*, 1492–1510.